

1 Supplemental Information Appendix

2

3 Rapid deposition of oxidized biogenic compounds to a temperate forest

4

5 Tran B. Nguyen,^{1†*} John D. Crouse,^{1‡} Alex P. Teng,¹ Jason M. St. Clair,¹ Fabien Paulot,^{3,4} Glenn
6 M. Wolfe,^{5,6} and Paul O. Wennberg^{1,2*}

7 1. Division of Geological and Planetary Sciences, California Institute of Technology,
8 Pasadena, California, USA

9 2. Division of Engineering and Applied Science, California Institute of Technology,
10 Pasadena, California, USA

11 3. Geophysical Fluid Dynamics Laboratory, National Oceanic and Atmospheric
12 Administration, Princeton, New Jersey, USA

13 4. Atmospheric and Oceanic Sciences, Princeton University, Princeton, New Jersey, USA

14 5. Atmospheric Chemistry and Dynamics Lab, NASA Goddard Space Flight Center,
15 Greenbelt, Maryland, USA

16 6. Joint Center for Earth Systems Technology, University of Maryland Baltimore County,
17 Baltimore, Maryland, USA

18

19

20 [†]*TBN and JDC contributed equally*

21 *Correspondence to T.B. Nguyen (tbn@caltech.edu) and P.O. Wennberg (wennberg@caltech.edu)

22

23

24

1 **1. Site and Campaign**

2 This research was conducted during the Southern Oxidant and Aerosol Study (SOAS)
3 ground campaign that occurred from June – July 2013 in Alabama and Tennessee. SOAS
4 was part of the larger Southern Atmosphere Study (SAS) campaign, which encompassed
5 many sampling sites and included multiple measurement platforms (tower, ground, and
6 aircraft). Both SOAS and SAS focused on understanding biosphere-atmosphere interactions
7 in the Southeastern United States. The SOAS site was located near Brent, Alabama at the
8 Centreville (“CTR”) Southeastern Aerosol Research and Characterization Study (SEARCH)
9 location managed by the Electric Power Research Institute (Latitude 32.90289 Longitude -
10 87.24968) for the U.S. Environmental Protection Agency, and is hereinafter referred to as
11 CTR. During the campaign, CTR experienced typically humid (RH 50 – 80%) and warm (28
12 – 30 °C) conditions in the daytime. Winds were observed from all directions; however, the
13 predominant winds were southerly during this experiment. The CTR site was surrounded on
14 three sides (N, W, and E) by a temperate forest that is part of the Talladega National Forest
15 and on the southern side by a grassy field. The forest canopy was comprised of needle-leaf
16 coniferous (shortleaf, longleaf, and loblolly pine) and broad-leaf deciduous (primarily oak,
17 sweetgum, and hickory) tree species. The mean canopy height was approximately 10 m. A 20
18 m metal walk-up tower was erected in the field several meters from the edge of the forest.
19 The instrument used for this work was stationed at the topmost platform of the tower with the
20 inlet facing north. The measurement height (z) was approximately 22 m, including the sensor
21 heights. Section 2 describes the instrumentation employed in this work in more detail. The
22 mass spectrometers, pumps, and computers were housed in an insulated enclosure that was
23 temperature-controlled with an HVAC unit to protect the components from precipitation and
24 large temperature swings. The sonic anemometer was mounted on top of the instrument
25 enclosure, extending approximately 2 meters north. The sonic was collocated laterally but
26 separated longitudinally from the inlet approximately 0.8 m (see Section 5, standard
27 corrections).

28 **2. Measurements**

30 **Chemical ionization mass spectrometry (CIMS):** Gas-phase compounds were measured
31 with negative-ion chemical ionization mass spectrometry (CIMS) using CF_3O^- as the reagent

1 ion, described in more detail previously (1-3). The CF_3O^- ionization is sensitive toward acids,
2 hydroperoxides, multifunctional nitrates, and multifunctional compounds. Hereinafter the
3 measurement technique will be referred to simply as “CIMS” for brevity. Analytes are
4 generally ionized via two different mechanisms:



7 The fluoride transfer mechanism occurs for acidic analytes AH (e.g., nitric or formic
8 acids), resulting in an ion with $m/z = \text{MW} + 19$. The cluster formation mechanism occurs for
9 all other analytes M (e.g., H_2O_2 , organic nitrates, hydroxy carbonyls, etc.), resulting in an ion
10 with $m/z = \text{MW} + 85$. Weakly acidic analytes will be ionized via both mechanisms, but their
11 fluoride transfer ions are used for quantification due to higher sensitivity and fewer
12 interferences. CIMS calibration and analysis methods are presented in Section 3.

13 The mass analyzer was a compact time-of-flight (TOF, ToFwerk) spectrometer with
14 mass resolving power of 800 $m/\Delta m$ and a mass accuracy of < 100 ppm. The measurement
15 rate of 10 Hz was employed for this work. Ambient air was sampled through a 3.1 cm inner
16 diameter inlet, comprising of a 43 cm long glass section then a 17 cm glass section that both
17 coated with a layer of Fluoropel hydrocarbon film (to minimize wall interactions), at a flow
18 rate of 2000 std. L min^{-1} . From the center of the high inlet flow, ~ 180 std. mL min^{-1} was
19 subsampled for the analytical flow, using a moving aperture which was continuously
20 adjusted to maintain 35.0 hPa pressure in a short Fluoropel-coated glass flow tube, as
21 described previously (1). The ambient air stream was diluted a factor of 9 – 11 with dry
22 nitrogen gas before entering the ion-molecule flow region, in order to moderate the effect of
23 water vapor on ionization sensitivity (Section 3). The mixing ratios reported have been
24 corrected for the dilution factor.

25 An ambient zero background (ambient air that has been scrubbed of reactive volatile
26 compounds by bicarbonate-impregnated nylon wool and Palladium-Alumina catalysts) and a
27 dry zero background (dry nitrogen from liquid N_2 boil-off) were recorded every 30 minutes.
28 Ambient calibration (a total flow of 92 std. mL min^{-1} of dry nitrogen carrying calibration gas
29 joined with the ambient zero flow) and dry calibration (the same calibration gas stream
30 joined with the dry zero flow) were recorded every 2 hours. These in-field calibration
31 standards are derived from (a) permeation tubes of isotopically-labeled formic acid

1 (H¹³COOH), acetic acid (¹³CH₃¹³COOH), and nitric acid (H¹⁵N¹⁸O₃) kept at 50°C, (b)
2 hydrogen peroxide (H₂O₂) from a urea hydrogen peroxide ((NH₂)₂CO·H₂O₂) standard kept at
3 0°C, and (c) diffusion vials of deuterium-labeled methyl hydroperoxide (CD₃OOH) and
4 peroxyacetic acid (CH₃C(O)OOH) kept at 0°C. The calibrations at ambient and dry RH were
5 used to validate laboratory-derived water-dependent calibration factors, which were
6 performed with a larger water vapor range, for the select compounds.

7
8 **Sonic Anemometer:** A three-dimensional ultrasonic anemometer (Campbell Scientific,
9 model CSAT3, hereinafter “sonic”) was used to measure the wind speeds and the speed of
10 sound along three non-orthogonal sonic axes. The wind speeds were transformed by the
11 analyzer to the orthogonal wind velocity components u , v , and w . The effects of wind
12 blowing normal to the sonic path were corrected online. The speed of sound in moist air was
13 converted to the sonic virtual temperature offline by applying a temperature- and humidity-
14 dependent correction function (4). The data from the sonic was sampled at 8 Hz frequency.

15 **Weather Station:** Meteorological conditions were continuously monitored by a weather
16 station (Coastal Environmental Systems Inc, Zeno® 3200) mounted on top of the CIMS
17 enclosure at the top of the tower. Air temperature (T, °C) and relative humidity (RH, %) were
18 monitored by the S1276Z sensor with ± 0.4 °C accuracy for T and $\pm 3\%$ for RH. Barometric
19 pressure (P, mBar) was monitored by the S1080Z sensor with ± 0.3 mBar accuracy. Solar
20 radiation (W m⁻²) was monitored by the LI-COR LI200SZ pyranometer sensor with $\pm 10\%$
21 accuracy. Wind speed (m s⁻¹) and wind direction (0 – 360°) were measured by the S1146Z
22 cup and vane sensor with accuracy of ± 5 m s⁻¹ for wind speed and $\pm 5^\circ$ for direction. Wind
23 direction of 180° is interpreted as northerly.

24 3. CIMS Calibration and Data Analysis

25 **a. Sensitivity and water-dependence calibrations** The sensitivities of CIMS to specific
26 analytes are controlled by physical characteristics such as their dipole moments and
27 polarizability (5). There are varying degrees of water-dependence in the ionization of
28 each compound, which becomes more significant for those that form weaker clusters with
29 the anion. For compounds for which authentic standards were commercially available or
30 can be synthesized, a water-dependent sensitivity calibration was performed in the

1 laboratory prior to ambient measurements. For other compounds, theoretical calculations
2 were performed to estimate the sensitivity, as described in more detail elsewhere (6). The
3 molecular identities, abbreviations used in this work, methods of calibration, and
4 estimated measurement error for each compound are reported in Table S1. Representative
5 traces of CIMS compounds and vertical wind w are shown in Figure S1, illustrating
6 different propensities toward turbulent transfer for these compounds. The mixing ratio of
7 water is anti-correlated with H_2O_2 and ISOPOOH+IEPOX, visually demonstrating the
8 different directions of their net flux. The magnitude of the fluctuations, e.g., of H_2O_2 (\pm
9 50%) and to ISOPN ($\pm 15\%$), are indicative of the magnitude of their biosphere-
10 atmosphere exchange velocities.

11 Authentic standards were used to characterize the dependence of the CIMS sensitivity to
12 water vapor by introducing a gas stream containing a known quantity of the calibrant
13 compound to the CIMS flow region while varying the amount of water vapor that is co-
14 introduced. Variable water vapor content was achieved by mixing different ratios of dry
15 nitrogen with a gas stream containing $\sim 3\%$ water vapor. The water vapor fraction was
16 characterized by Fourier-transform infrared spectroscopy (FTIR) with a 19 cm pathlength
17 cell. Spectral fitting for water vapor was performed using the HITRAN spectral database
18 (7) and a nonlinear fitting software NLM4 (8). The quantifications of other calibrant
19 gases were performed as follows:

- 20 1) HCN was calibrated with a standard gas mixture (6.3 ppmv in N_2 , Scott Specialty
21 Gasses) that was diluted with a known flow rate of dry nitrogen.
- 22 2) H_2O_2 was calibrated by flowing dry nitrogen continuously over urea hydrogen
23 peroxide (Aldrich, purity 97%), kept at 0°C . Absolute H_2O_2 mixing ratio in this
24 stream was quantified by bubbling the equilibrated outflow into ultrapure water (18
25 $\text{M}\Omega$, Millipore) for a fixed time. The aqueous H_2O_2 was quantified by high-
26 performance liquid chromatography (HPLC) mass spectrometry, as well as a UV-
27 Visible colorimetric technique (3).
- 28 3) Formic acid (Aldrich, 98%) and nitric acid (Aldrich, 70% in water) were calibrated
29 by flowing dry nitrogen continuously over permeation tubes (Kintec), kept at 50°C .

1 The permeation rate was determined by gravimetric analysis for formic acid. Nitric
2 acid permeation was calculated by collecting the outflow in ultrapure water and
3 analyzing the solution with ion-chromatography (IC).

4 4) PAA (Aldrich, 40% in water) was calibrated by flowing dry nitrogen continuously
5 over custom diffusion vials, kept at 0°C, and collecting the outflow similarly to the
6 protocol for H₂O₂. The outflow solution was analyzed by HPLC-derivatization
7 fluorescence. Additionally, gas-phase PAA was analyzed with FTIR using the IR
8 cross section from Orlando et al (9).

9 5) HMHP was synthesized in the gas phase by the reaction of H₂O₂ and formaldehyde
10 and characterized by FTIR as described by Fry et al (10).

11 6). Hydroxyacetone (Aldrich, 90%) was introduced into an evacuated 500 mL glass
12 bulb by monitoring pressure increase, and backfilled with dry N₂ to obtain several
13 ppmv. This mixture was quantified by FTIR using the cross section archived in the
14 Pacific Northwest IR Database (11). The gas in the IR cell was introduced into a ~
15 300 L Teflon bag and diluted with zero air.

16 7) The sum of ISOPOOH and IEPOX were observed at the product ion with m/z 203
17 as they are isobaric (C₅H₁₀O₃). IEPOX was synthesized as reported in Bates et al
18 (12). A measured weight of a standard solution of IEPOX in water was atomized
19 into a 24 m³ FEP Teflon bag alongside hydroxyacetone and toluene as a volume
20 tracer (that was quantified by GC-FID), as reported recently (13). The vapor wall
21 loss and solution-phase decomposition for this method were characterized to be
22 negligible. The combined sensitivity was then determined from a photooxidation
23 experiment, with the assumptions of yields as reported in Paulot et al (14).

24 8) ISOPN was synthesized and calibrated as outlined by Lee et al (15). The calibration
25 method relied on the quantitative thermal dissociation of the organic nitrate to NO₂
26 followed by laser-induced fluorescence quantification of NO₂ (TDLIF instrument).

27 9) PROPNN, and the sum of MACN + MVKN were generated as part of a high-NO
28 isoprene oxidation and separated with a GC column, as described by Lee et al (15).

1 The outflow of the GC column was directed toward CIMS and the TDLIF
2 instruments, and the calibration technique was similar to that of ISOPN.

3 **b. Measurements of water vapor:** High-frequency water vapor mixing ratios for the
4 calculations of latent heat fluxes were determined by CIMS, using the double cluster ion
5 $(\text{H}_2\text{O})_2\cdot\text{CF}_3\text{O}^-$ (m/z 121). This ion remained linear with respect to the range of water
6 vapor mixing ratios experienced at SOAS while the primary water ion $(\text{H}_2\text{O})\cdot\text{CF}_3\text{O}^-$ was
7 saturated. The $(\text{H}_2\text{O})_2\cdot\text{CF}_3\text{O}^-$ ion had a considerable temperature dependence that was
8 corrected for as a function of the measured flow tube temperatures. Atmospheric water
9 vapor, as measured by the Zeno weather station at 1 Hz, was used as an absolute
10 calibrant. Atmospheric water vapor was calculated from the observed barometric
11 pressure, air temperature, and relative humidity for all dates included in the study (Fig.
12 S2) and the corrected CIMS water vapor measurements compared well to the weather
13 station measurements (Fig. S3.)

14 15 **4. Eddy Covariance (EC) calculations**

16 **a. Data processing:** EC fluxes were calculated after the signals of the compounds measured
17 by CIMS (x , shown in Table S1) were converted to mixing ratios (usually in pptv) by
18 applying all calibrations and corrections. Given the wind velocity vectors (u, v, w) and
19 scalar matrices for species of interest, flux data for virtual temperature $(\overline{w'T_v'})$,
20 momentum $(\overline{w'u'})$, and CIMS-determined compounds including water vapor $(\overline{w'x'})$ were
21 calculated for each ~ 30 minute flux measurement periods, where primes denote
22 deviation from the mean and overbars denote a mean over the flux period. Large spikes in
23 CIMS signals, caused by electronic or temperature instability, were removed by
24 referencing a “quiet” m/z , where no chemical signal is found, and by visual inspection (<
25 5% of data). For each period: the 8 Hz wind measurement was interpolated onto the time
26 vector of the CIMS measurement, the sonic wind velocity coordinates were rotated by a
27 two-step rotation so that $\overline{v}=0$ and $\overline{w}=0$, the sonic data and CIMS data were detrended
28 using a linear detrending algorithm, the correction of inlet lag of the scalar signal of x'
29 was corrected for lag with respect to w' by identifying the peak in the lag-covariance
30 function (Fig. S4). Lag times were on the order of 0.1 – 1.1 s. The lag time for H_2O was

1 used as the representative lag time for all compounds, which was justified by inspecting
2 the cross covariance spectra for multiple CIMS species for more than 10 daytime flux
3 periods. Using a representative lag time from a compound whose scalar vector has a large
4 covariance with w , was found to decrease the uncertainty of the resulting EC fluxes
5 propagated from the error in locating poorly-defined extrema in the cross covariance
6 spectra for periods of lower flux (e.g., nighttime) or for compounds where the covariance
7 is small (e.g., MTNP). The instantaneous fluxes were then averaged over each flux
8 period. Mean concentrations and solar radiance data were averaged over the same
9 periods.

10 **b. Quality of flux data**

11 The EC fluxes were screened according to the following criteria: i. The upward and
12 downward energy fluxes at the surface should be balanced within the standard deviation
13 of each measurement ($\sim 15\%$ in the daytime), ii. The spectral analysis should indicate
14 expected behavior of the individual covariances with respect to eddy magnitudes and
15 surface layer theory; iii. The turbulence should be well developed for the day time
16 periods; iv. The stationarity (16) and intermittency (17) conditions should be met.
17 Condition i severely limited the number of useable days within the campaign for
18 calculations of EC fluxes from CIMS. The quality analysis for Conditions ii - iv below
19 pertains mainly to days where EC fluxes were deemed acceptable per Condition i.

20 **i. Energy balance closure condition:** The degree of surface energy balance closure
21 provides an important and objective evaluation of the EC fluxes, as conditions
22 that violate EC flux assumptions (e.g., contamination of vertical flux from
23 horizontal wind due to effects of roughness layer inhomogeneity) should affect
24 the turbulent transfer of energy similarly to mass. An external calibration
25 (pyranometer measurements of radiation) was used to constrain the closure
26 condition. The surface energy balance can be written as:

$$27 \quad R_n = SH + LE + S + G + Q \quad (3)$$

28 where R_n is the net radiation downward, SH is the sensible heat flux, LE is the
29 latent heat flux, S is the storage heat flux, G is the soil heat flux, and Q
31

1 collectively represents all other energy fluxes. Q is generally a small term and was
2 ignored in this work. We also make the assumption that the canopy is closed, so
3 that G can also be ignored. The revised energy balance equation is written as:
4

$$5 \quad R_n - S = SH + LE \quad (4)$$

6
7 And the heat fluxes are defined as:
8

$$9 \quad SH = \rho_a c_p \overline{w'T_v'} \quad (5)$$

$$10 \quad LE = \rho_a L_v(T) \overline{w'x_{H2O}'} \quad (6)$$

11 where ρ_a is the density of air (kg m^{-3}), c_p heat capacity of air ($\text{J kg}^{-1} \text{ }^\circ\text{C}^{-1}$) at 1 atm,
12 $L_v(T)$ is the latent heat of vaporization of air (kJ kg^{-1}) calculated for the
13 temperatures experienced throughout the flux period, and x_{H2O} is the water vapor
14 fraction as determined by CIMS (described in Section 3a). The storage term S was
15 not measured, but was estimated based on measurements at a similar site (18). S is
16 usually small ($-20 - 50 \text{ W m}^{-2}$) and thus, error in its estimation does not add
17 significantly to the error of the analysis. Our pyranometer measures solar
18 radiation (shortwave radiation downward) whereas net radiation includes the
19 upwelling and downwelling shortwave and longwave radiation ($R_n = SW_{\text{up}} +$
20 $SW_{\text{down}} + LW_{\text{up}} + LW_{\text{down}}$). As longwave radiation was not measured, R_n was
21 estimated with a method similar to the treatment of satellite data, by exploiting
22 empirical relationships between net radiation and shortwave radiation as
23 developed by Kaminsky et al (19). It was shown that the error in this type of
24 estimation is small ($r^2 = 0.96 - 0.99$, root mean square error $18 - 41 \text{ W m}^{-2}$)
25 compared to the typical magnitude of R_n (up to 1000 W m^{-2}).

26 One of the largest influence on energy balance closure for our work
27 appeared to be wind direction, as southerly winds were typically associated with
28 poor balance closure and northerly winds, even with contributions from winds
29 originating from the west and east, were associated with satisfactory balance
30 closure for the individual day (Fig. S5). This strong impact by wind direction is
31 likely related to the challenges of EC flux measurements from a walk-up tower
(e.g., tower and/or instrument enclosure acting as physical barriers that isolate the

1 inlet and sonic from southerly winds) and the change in roughness element or
2 topology due to the transition from the forest in the north, west, and east
3 directions toward the grassy field to the south.
4

5 **ii. Spectral analysis:** The cospectra of x and T_v with w in the frequency domain
6 were calculated by applying a fast Fourier transform to the covariance matrices.
7 Figure S6 shows the averaged cospectral densities of several CIMS compounds,
8 chosen for those with higher signal-to-noise to limit error, and T_v with w for the
9 afternoon local hour 13 on all days included in this flux study. If the
10 homogeneous fetch is adequate, an underlying assumption for EC, there should be
11 a development of an “inertial sublayer,” where the fluxes of conserved scalars
12 (e.g., energy) are roughly independent of vertical height. The spectra show the
13 expected linear falloff in the inertial subrange frequency ($f > 0.003$ Hz) and, for
14 the averaged CIMS compounds, the typical slope is similar to the $f^{-7/3}$ slope
15 predicted by surface layer theory (20). For virtual temperature, the linear falloffs
16 for some cospectra were shallower than $f^{-7/3}$, but never shallower than $f^{-5/3}$, such
17 that the average for all days was most similar to an $f^{-6/3}$ slope.

18 The plots of cumulative distribution of cospectral density (ogives) indicate
19 the frequency ranges where most of the flux is captured. Figure S7a shows the
20 representative ogives for w with several CIMS compounds and T_v , for the
21 afternoon local hours 9 – 15 of all days included in this flux study and Figure S7b
22 shows the data for JD165. The spectra were normalized to their asymptotic value
23 in the low-frequency range. As expected, the ogives approach horizontal
24 asymptotes at both ends of the spectrum. In the high-frequency end, there was no
25 more flux at approximately 1 Hz, which indicates that the measurement
26 timescales used in this work (10 Hz for CIMS species and 8 Hz for winds) was
27 sufficiently fast to capture fluxes carried from the smaller eddies (timescales of 10
28 s). In the low-frequency end, all of the flux was carried by eddies of frequencies
29 higher than 1×10^{-3} Hz. This indicates that, as an ensemble, our averaging time of
30 30 minutes was long enough to capture the entirety of the flux. The $w'x'$ ogive
31 decreases more quickly than the $w'T_v'$ ogive. This is perhaps a real characteristic,

1 as suggested by an earlier study of acyl peroxyxynitrate (APN) compounds at
2 BEARPEX (21), because the spectra are similar for compounds whose instrument
3 time response delays were small (Section 5).

4 Figure S8 shows the frequency-weighted covariance-normalized cospectra
5 plotted against $n = fz/U$, where z is the measurement height and U is the average
6 wind speed for the day. The spectra for (a) JD165 and (b) all days included in the
7 study show one distinct maximum corresponding to $n \sim 0.2 - 0.4$ and few
8 complex turbulent structures, indicating that most of the flux was carried by
9 eddies of timescale ~ 30 s. The slope for CIMS compounds was steeper than for
10 T_v in the high frequency domain, also observed for APNs at BEARPEX (21).
11 Combined, the spectral analysis for the species reported in this work provides
12 compelling evidence that the calculated EC fluxes during the daytime hours are
13 accurately represented.

14
15 **iii. Turbulence:** The criterion requiring well-defined turbulence can be accessed by
16 examining the friction velocity u_* , calculated in this work from the measured
17 momentum flux ($\tau = -\rho_a \overline{w'u'}$), where ρ_a is the density of air (kg m^{-3}):

$$u_* = |\tau/\rho_a|^{1/2} \quad (7)$$

18 Figure S9 shows u_* averaged for all days included in this study and errors are one
19 standard deviation from the mean. The determination of turbulent threshold
20 u_* values is subject to debate and may be site-specific. For periods where
21 conditions can be characterized as turbulent, the calculated EC fluxes are affected
22 by substantially fewer errors than for calm periods. Threshold values of $0.1 - 0.3$
23 m s^{-1} have been suggested, and a median value of 0.23 m s^{-1} that was found to be
24 most representative of multiple sites and years (22) was used in our work to
25 qualitatively assess if daytime periods can be characterized as turbulent and
26 further validate the flux data. It was found that, for days with good energy
27 balance, the criterion was satisfied within the standard deviation of the
28 u_* measurement.

1 **iv. Stationarity and Intermittency:** The stationarity test was performed as
2 suggested by Foken and Wichura (16), where flux data (F) were calculated for 5
3 min averaging periods in addition to 30 min averaging periods. When both
4 calculations were averaged into the same 30 min time bin, the resulting
5 stationarity criterion ($FS < 0.3$), defined as $FS = |F_{30\text{min}} - F_{5\text{min}}|/F_{30\text{min}}$, was
6 satisfied for the majority of points in the day time periods. The stationarity
7 criterion was used as a qualitative assessment and not a discrimination threshold
8 in this work as the available data are sparse. Figure S10 shows the stationarity
9 analysis for H_2O_2 and sensible heat on JD165, where the 5 min data averaged
10 similarly to the 30 min data did not significantly alter the result. The intermittency
11 criterion (17), defined as $FI = \sigma_{5\text{min}} / F_{30\text{min}}$ where $\sigma_{5\text{min}}$ is the standard deviation in
12 the 5 minute data, was satisfied ($FI < 1$).

14 5. EC flux corrections:

15 **Standard corrections:** Corrections that are often recommended for EC flux
16 calculations (23) were systematically applied in this work where appropriate. Despiking, time
17 lag, and coordinate rotation were performed as discussed in Section 4a. Cross-wind
18 corrections were applied online within the CSAT3 sonic electronics. The effects of
19 temperature and humidity on the measured air temperature, e.g., buoyancy, were removed in
20 the calculation of the virtual temperature from the sonic speed of sound. Corrections due to
21 flux attenuation at high frequencies were unnecessary as the CIMS measurement was fast
22 enough to capture all the flux in the high-frequency range (Fig. S7a). Webb-Pearman-
23 Leuning (WPL) corrections (24) were unnecessary as we measured the mixing ratio not the
24 partial pressure of chemical species, and temperature and humidity corrections to CIMS
25 sensitivities needed to output count signals to pptv were applied internally as a standard
26 procedure. Transfer functions used to correct for the potential loss of flux due to the
27 separation of the inlet (Fig. S7b) were calculated as suggested by Moore et al (25) but were
28 not applied because the error was estimated to be small ($\sim 3\%$ for CIMS compounds).
29 Corrections often reserved for open-path analyzers were not performed for the closed-system
30 CIMS measurements.

Instrumental time response correction: It is challenging to accurately measure compounds that have a propensity to interact with instrument surfaces in complex ways. HNO₃ is of particular concern for our instrument, and we discuss here correction for the loss of flux owing to a “smearing” effect of the HNO₃ signal in time from the interaction with instrument surfaces. The correction was based on observed instrumental responses for HNO₃, and a few other compounds where calibration standards were available in the field during SOAS. An exponential decay curve ($\alpha \cdot \exp(-t/\tau)$) was fit to periods following a pulse of the calibrant gas through the CIMS flow region, where τ (s) is the inlet time response constant and α is the pre-exponential factor. Figure S11 shows the decay curves for HNO₃ ($\tau = 32$, $\alpha = 0.55$), formic acid ($\tau = 0.94$, $\alpha = 0.80$), H₂O₂ ($\tau = 1.3$, $\alpha = 0.70$), and water vapor ($\tau = 0.22$, $\alpha = 1.06$) pulses. The fitted parameters for HNO₃ can be used to “degrade” signals with fast time responses (e.g., H₂O₂) and recalculate the fluxes by applying the smearing perturbation to the measured mixing ratios for each α and τ of interest. The adjusted mixing ratio $C(t)$ can be written as:

$$C(t) = X_t(1 - \alpha) + \alpha \cdot \frac{\int_{t-2\tau}^t X_i \cdot \exp\left(-\frac{(t-t_i)}{\tau}\right) \cdot dt_i}{\int_{t-2\tau}^t \exp\left(-\frac{(t-t_i)}{\tau}\right) \cdot dt_i} \quad (8)$$

where t_i is the time in seconds at each iteration i , and X is the observed mixing ratio of the chemical species. Figure S12 shows the results of applying various τ , while fixing α , to the H₂O₂ mixing ratio vector. A 1s time delay does not visibly change the observed H₂O₂ mixing ratio but longer time responses noticeably degrade the signal such that the high-frequency variations are damped. By design, the smearing function conserves signal.

We applied the smearing perturbation of HNO₃ ($\tau = 32$ s, $\alpha = 0.55$) to the EC calculations of H₂O₂, formic acid, and latent heat. We find that mean chemical mixing ratios do not change more than a few percent until time constants approach 1 or more hours (the timescale of diurnal variation); however, fluxes were affected for time constants on the order of seconds. Figure S13, top panels, shows that the H₂O₂ flux is significantly decreased from a signal degradation in the instrument, the mean concentration remains unperturbed, and, thus, the deposition velocity is significantly suppressed. The ratio of the undamped vs. damped values in V_d and fluxes ranged from 1.5 – 1.8 for multi-day analysis of the formic acid, H₂O₂,

1 and LE flux (Fig. S13, bottom panels). An average value of 1.62 was used to correct the
2 HNO₃ flux to the value that would have been measured if the time response constant for
3 HNO₃ was $\tau < 1$ s for all of the days included in this study. The mean mixing ratio values
4 were uncorrected. We note that the analysis only includes dampening caused in the CIMS
5 flow tube region, where the majority of the residence time is expected for our instrument. It
6 is possible that the inclusion of the fast flow (~ 2000 L min⁻¹) inlet interaction will require
7 greater dampening corrections; however, we do not have time decay data for compounds
8 through this section of the inlet (the chemical pulse would need to be at the tip of the inlet).
9 The correction for HNO₃ closes the gap between the measured and modeled V_d .

10 We further explored the effect of the time constant magnitude on the ratio of the
11 undamped vs. damped fluxes using realistic time constants ($\tau = 1 - 100$ s) for CIMS. This
12 time range is also relevant to eddy scales carrying most of the flux we measured, where the
13 loss of flux becomes especially important. Figure S14 shows that as τ increases, the ratio of
14 damped vs. undamped V_d decrease, as expected, but the decrease is not linear (Fig. S14
15 insert panel). For $\tau = 1$ s, greater than 98% of the H₂O₂ flux is conserved and for $\tau = 180$ s,
16 half of the flux is gone which leads to a significant underestimation in the calculated V_d
17 values. Interestingly, most of that flux was lost between 1 and 32 seconds. Flux loss due to
18 chemical interactions with surfaces is expected to be important for other “sticky” compounds
19 like NH₃ and IEPOX, where a similar correction may be needed.

20 For most of the CIMS compounds included in this work, time delays are expected to
21 be small (on the order of 1 s) with, perhaps, the exception of IEPOX. Unfortunately, we do
22 not have field calibration sources for all compounds for which to attempt a damping analysis.
23 For the combined ISOPOOH +IEPOX flux, ISOPOOH comprise greater than 66% of the
24 mixing ratio signal for most cases. However, the combined V_d may still be underrepresented
25 by our measurements if the IEPOX has time constant close to that of HNO₃.

26 27 **6. Resistance Model**

28 Many compounds detectable by CIMS were observed to have relatively high
29 deposition velocities, suggesting a small or negligible resistance to surface uptake by plant
30 stomatal or non-stomatal components such as leaf cuticles. We calculate the expected

1 contributions to deposition using a parameterization of surface deposition suggested by
 2 Wesely and Hicks (29), assuming a resistance-in-series scheme that considers the
 3 aerodynamic resistance (R_a), molecular diffusion resistance (R_b) and surface resistance (R_c)
 4 to the canopy that is parameterized as a large leaf:

$$V_d = \frac{1}{R_a + R_b + R_c} \quad (9)$$

5 R_a describes turbulent transfer of mass in the mixed layer to the surface, and can be
 6 parameterized by:

$$R_a = \frac{1}{ku_*} \left[\frac{k\bar{U}_{(z-d)}}{u_*} - \psi\left(\frac{z}{L}\right) \right] \quad (10)$$

7 where $\bar{U}_{(z-d)}$ is the mean wind speed at a height equal to the measurement height (z) less the
 8 displacement height (d , i.e., thickness of the “leaf”), u_* is the friction velocity (m s^{-1} , see Eq.
 9 7), k is the dimensionless von Kármán constant (0.4), $\psi\left(\frac{z}{L}\right)$ is a correction function for the
 10 sensible heat and momentum fluxes that is dependent on the dimensionless parameter z/L
 11 often used to characterize atmospheric stability. The formulation of $\psi\left(\frac{z}{L}\right)$ for the unstable
 12 period (local h = 9 – 15) was used to obtain the daytime R_a (30). L is the Monin-Obukhov
 13 length, defined as:

$$L = \frac{u_*^3 \bar{\theta}}{kg \overline{w'\theta'}} \quad (11)$$

14 where $\bar{\theta}$ is the mean potential temperature (K), i.e., the temperature of an air parcel
 15 transported adiabatically to surface pressure as calculated from the measured virtual
 16 temperature and atmospheric pressure, $\overline{w'\theta'}$ is the potential temperature flux, and g is the
 17 acceleration due to gravity (m s^{-2}).

18 R_b describes the diffusion of molecules through the quasi-laminar layer at the surface
 19 of the roughness element. R_b was modeled following the parameterization suggested by
 20 Jensen and Hummelshøj (31, 32) that included a direct dependence on leaf area index (LAI)

1 and the characteristic leaf thickness scale in the mixed-vegetation canopy (l , taken to be
2 0.001 m (31)):

$$R_b = \frac{\nu}{D_x u_*} \left[\frac{100 l u_*}{(LAI)^2 \nu} \right]^{1/3} \quad (12)$$

3 ν is the viscosity of air ($\text{m}^2 \text{s}^{-1}$) at the ambient pressure of the measurement height, and D_x is
4 the diffusivity of a molecule x in air. $D_{\text{H}_2\text{O}_2}$ was taken to be $1.56 \times 10^{-5} \text{ m}^2 \text{ s}^{-1}$ at 25°C (scaled
5 from measured values at 60°C (33)), and D_x for other molecules in this study was calculated
6 from $D_{\text{H}_2\text{O}_2}$ using Graham's Law, where $D_x = D_{\text{H}_2\text{O}_2} (\text{MW}_{\text{H}_2\text{O}_2}/\text{MW}_x)^{1/2}$. Table S4 shows the
7 diffusivity coefficients and other parameters used in the model for chemical species included
8 in this study and the results of the model.

9 LAI was measured during the SOAS campaign for the CTR site by coauthor G.M.
10 Wolfe with help from C.J. Groff (Purdue University). Measurements were performed using
11 an upward-looking light sensor (LAI-2000 Plant Canopy Analyzer) that measures the diffuse
12 radiation attenuation, i.e., the fraction of sky blocked by canopy elements, within the canopy
13 at multiple viewing angles. The attenuation is a function of total leaf area and average leaf
14 angle. A representative value ($\text{LAI} = 4.7$) was taken as the mean along three transects at
15 different orientations.

16 The average R_a value for the site on day 165 (June 15) was calculated to be $\sim 8 \text{ s m}^{-1}$
17 and R_b for H_2O_2 was $\sim 12 \text{ s m}^{-1}$. From the R_a and R_b values calculated, we find that the
18 residual resistance ($1/V_{d, \text{meas.}} - R_a - R_b$) is heavily-dependent on the solubility (e.g., the
19 Henry's Law coefficient (H)), with an additional dependence on the molecular mass of the
20 individual compounds. That the residual resistance depends on solubility suggests that the
21 bulk of this resistance is due to surface uptake. To model the surface resistance, we adjust the
22 original parameterization by Weseley (27). The Weseley parameterization incorporates the
23 dependence of R_c on molecular mass (e.g., diffusivity) in the stomatal resistance term (r_s)
24 and on H in the mesophyll (r_m) and cuticular (r_{cut}) resistance terms. The canopy was
25 assumed to be closed, and thus only the surface resistance from the canopy top was
26 considered, i.e., neglecting contributions from the soil and "lower canopy."

$$R_c = \left(\frac{1}{(r_s + r_m)} + \frac{1}{r_{cut}} \right)^{-1} \quad (13)$$

1 An adjustment to the Weseley parameterization was necessary because the original scheme
 2 overestimate R_c for H_2O_2 and HNO_3 in our work (demonstrated by various experimenters and
 3 in this work to be less than 5 s m^{-1} (34, 35)). Other evaluations of observed vs. modeled H_2O_2
 4 flux in a forest (36) similarly concluded that the original Weseley scheme overestimated R_c
 5 for H_2O_2 . Coefficients in the parameterizations of r_m and r_{cut} were empirically revised to
 6 close the discrepancy. We demonstrate that the revised parameterization successfully predicts
 7 R_c for not only H_2O_2 and HNO_3 , but also for the series of organic and inorganic compounds
 8 studied in this work. Further validation is needed before this revised Weseley scheme can be
 9 generally applied for all compounds, at all sites, and for all seasons. The resistances to leaf
 10 components can be written as:

$$r_s = \left(\frac{D_{H_2O}}{D_x} \right) r_{H_2O} \quad (14)$$

$$r_m = \left(\frac{H}{50RT} + 100f_0 \right)^{-1} \quad (15)$$

$$r_{cut} = (10^{-4}H/RT + f_0)^{-1} \quad (16)$$

11 where r_{H_2O} is the stomatal resistance to the diffusion of water, H is the Henry's Law
 12 coefficient (M atm^{-1}), R is the gas constant ($\text{atm M}^{-1} \text{K}^{-1}$), T (K) is the air temperature, and f_0
 13 is a reactivity factor (27) that is defined as 0 = non-reactive, 0.1 = semi-reactive and 1 =
 14 reactive as ozone. The values of D_x , H and f_0 used in this work are reported in Table S2.
 15 Values of f_0 were used as suggested by Weseley for available compounds, and set as 0
 16 otherwise. The r_{H_2O} term may be dependent on number variables, such as photosynthetically-
 17 active radiation, CO_2 air mixing ratio and assimilation, water fraction in the leaves and in the
 18 air, stomatal density, LAI, and air temperature. In the absence of measurements, only
 19 daytime values of V_d were calculated here, and daytime r_{H_2O} was assumed to be similar to
 20 the value computed at the BEARPEX campaign (21).

21 For many of the multifunctional compounds studied in this work, H is not known;
 22 thus, we estimate H based on chemical proxies. Uncertainties in H estimates, which can be >

1 100% due to the paucity of measurements, are critically important to the R_c term for certain
2 ranges of H (see Fig. S16 and related discussion). Thus, resistance model results should be
3 treated as a rough approximation in this work for compounds with unknown H . An example
4 of the large uncertainty in H is the trend with increasing carbon number for the family of
5 hydroxy nitrates. Shepson et al (37) found decreasing H for hydroxy nitrates of increasing
6 carbon number, whereas Treves et al (38) observed the opposite trend. H can be significantly
7 different for different isomers of the same compound; however, the trend of decreasing H
8 with increasing carbon number appears to be more consistent with observations of some
9 chemical families, e.g., in the family of $C_1 - C_9$ straight-chain aldehydes or $C_3 - C_{11}$ straight-
10 chain ketones ((39), and references therein). This trend may be rationalized because the
11 addition of a more hydrophobic alkyl group, while conserving the singular hydrophilic group
12 (e.g., aldehyde) should depress H if all else is equal.

13 Neither the Shepson et al nor the Treves et al H values can be applied directly,
14 however, as the nitrates we measured were not exclusively alkyl hydroxy nitrates, e.g.,
15 ISOPN is a hydroxy nitrate with an alkenyl group, PROPNN is a nitrate with a ketone or
16 aldehyde group, and MACN + MVKN are hydroxy nitrates with a ketone or aldehyde
17 groups. Thus, we used the Shepson et al H values, and extrapolated to higher carbon numbers
18 when necessary. The estimation for INP and MTNP are especially uncertain. As more
19 measurements become available due to greater availability of synthesized authentic
20 standards, the uncertainties in the resistance model can be revised downward. The modeled
21 resistances are shown in Fig. S15. Modeled R_c agree well with previous observations for
22 HNO_3 and H_2O_2 ($0 - 5 \text{ s m}^{-1}$), and ROOH ($20 - 40 \text{ s m}^{-1}$) (34, 35, 40). HCN is both observed
23 and calculated to have the largest total resistance to deposition. Further, R_c is the largest
24 component of the summed resistance for HCN, due to its small H value.

25 Here we estimate the sensitivity of the resistance model to parameters such as LAI,
26 u^* and leaf thickness. A hypothetical $\pm 200\%$ change in these input parameters modified R_b
27 by $|37 - 58|\%$ and V_d by $\sim |25 - 30|\%$. This V_d model error is similar to standard deviation of
28 the measurements. At SOAS, our measurements of LAI in particular, performed from
29 6/18/2013 – 6/20/2013 at viewing angles $90 - 270$ degrees at three locations within the forest
30 had a 2-sigma uncertainty of 35% (for a confidence level of 95%). This translates to an R_b

1 change of |18 – 33|% and a V_d change of |10 – 17|% in the resistance model, which is also
2 within the experimental uncertainty of the measurement. In contrast, H is a parameter where
3 estimates may vary by much larger margins due to the unavailability of direct measurements
4 for most OVOCs. We find that above a threshold value ($H > 3 \times 10^4 \text{ M atm}^{-1}$), the resistance
5 model we used becomes much less sensitive to increases in H . We can illustrate this idea by
6 comparing the calculated deposition velocities of two hypothetical water-soluble compounds
7 (X,Y) (high Henry’s Law coefficient, H) that are not reactive (low reactivity coefficient, f_0).
8 Compound Y is taken as the reference compound with $H = 1 \times 10^5 \text{ M atm}^{-1}$ and $f_0 = 0$. For
9 compound X, H is varied from 1×10^1 to $1 \times 10^8 \text{ M atm}^{-1}$. The fractional difference in
10 calculated V_d between X and Y is shown in Figure S16. It is clear that uncertainties in H are
11 very important in an intermediate regime (changing V_d by $\sim 80\%$), but at either extremes
12 (i.e., $H \rightarrow 0$ and $R_c \rightarrow \infty$, or $H \rightarrow \infty$ and $R_c \rightarrow 0$), the effect is muted.

13 7. GEOS-Chem Modeling

14 Global and regional model simulations are performed using the GEOS-Chem global
15 3-D chemical transport model v9–02 (26). The model is driven by GEOS-FP (“Forward
16 Processing”) assimilated meteorology with hourly resolution. This version of GEOS-Chem
17 implements a new isoprene oxidation mechanism (Mao et al (2013)) based on Paulot et al
18 (2009 a,b). We update this mechanism to include the results of recent studies performed by
19 our group and other groups (Table S3 and corresponding references). Several chemical
20 species measured at the site are not discussed because they are not currently included in the
21 standard mechanism (e.g., HCN, HMHP, HPALD, HDC₄, DHC₄, INP, and MTNP) or
22 because their dry deposition is not considered (PAA).

23 GEOS-Chem uses the resistance-based approach described by Wesely 1989 (27) to
24 calculate dry deposition velocities. The performance of this approach depends both on the
25 knowledge of meteorological drivers (e.g., atmospheric stability), surface conditions (e.g.,
26 LAI) and the solubility (effective solubility H^*) and reactivity (reactivity factor f_0) of the
27 compound of interest (Table S4). f_0 in the GEOS-Chem model is set to 1 for many VOCs to
28 reflect recent observations from Karl et al (28). We performed two types of simulations for
29 this work:

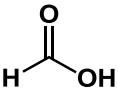
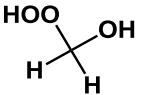
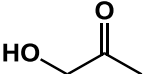
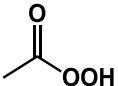
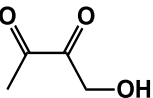
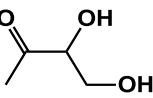
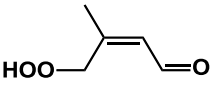
1 (1) **Regional simulation:** A set of simulations was performed to calculate dry deposition
2 velocities at CTR site using GEOS-FP meteorology at a horizontal resolution of resolution of
3 ($0.25^\circ \times 0.33^\circ$) over the contiguous US. We find that the GEOS-FP captures well the
4 observed wind speed, friction velocity, latent heat, and sensible heat fluxes at the CTR site.
5 Here we adjust H^* iteratively (Table S4) to improve the model agreement with observations
6 performed on June 15, 2013.

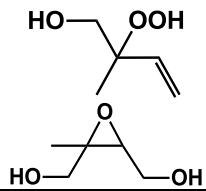
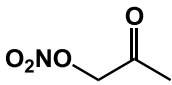
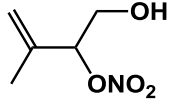
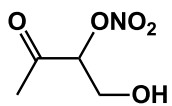
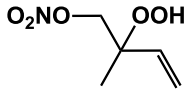
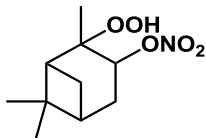
7 (2) **Global simulation:** Two global simulations ($2^\circ \times 2.5^\circ$) are performed for 2013 to
8 evaluate the impact of our improved dry deposition parameterization on the global budget of
9 selected tracers. The base simulation uses the dry deposition velocities (i.e., the H^*) currently
10 used by GEOS-Chem, while our sensitivity simulation arbitrarily increase H^* to match our
11 CTR observations of deposition velocities. Each simulation is preceded by a 4-month spin-
12 up. Monthly deposition fluxes, deposition velocities, and surface concentration of select
13 species are reported as monthly diurnal averages of one hour periods.

14 The sensitivity simulation suggests that deposition velocities at the CTR site are similar
15 to forests across the southeast and northeast U.S. For example, modeled daytime V_d for H_2O_2
16 across the eastern U.S. are $4 - 6 \text{ cm s}^{-1}$ (Fig. S18) compared with the $5.2 \pm 1.1 \text{ cm s}^{-1}$ measured at
17 CTR. Furthermore, the consistency between our observations of H_2O_2 deposition in a mixed
18 forest in AL and those measured at Canadian Boreal forests (18), German spruce forests (19),
19 and other forested sites in OR and TN (17) suggest that the results obtained here and elsewhere
20 for H_2O_2 may be representative of forests in general. It is possible that, for compounds like H_2O_2
21 where deposition happens with no surface resistance, and where dissociation equilibria on the
22 surface of plants are negligible, characteristics of the specific sites may be unimportant to
23 understanding daytime deposition. Additional flux observations of reactive trace gases will be
24 helpful to validate this suggestion. The year-round sensitivity simulation also shows that
25 deposition velocities and friction velocities observed during the campaign days are typical
26 summer values (Fig. S19) and high deposition rates can extend over much of the period between
27 spring and fall.

1
2
3
4
5
6
7
8

Table S1: Molecular identities, abbreviations, and CIMS calibrations of the chemical species included in this study. The molecular structures shown may represent one of many structural isomers that can be characterized as the same chemical species (e.g., IEPOX has 4 isomers) or different chemical species (e.g., DHC4 may be a ketone or aldehyde).

Compound	Abbrev.	Representative Structure	CIMS ion	Cal Method (see text)	Sensitivity uncertainty
Hydrogen cyanide	HCN	$\text{HC}\equiv\text{N}$	$(\text{HCN})\cdot\text{CF}_3\text{O}^-$	Commercial standard gas mixture	30%
Hydrogen Peroxide	H_2O_2	$\text{HO}-\text{OH}$	$(\text{H}_2\text{O}_2)\cdot\text{CF}_3\text{O}^-$	Commercial standard + HPLC	30%
Formic Acid	Formic		$(\text{HCOOH})\cdot\text{F}^-$	Commercial standard + gravimetric	20%
Nitric Acid	HNO_3	$\text{O}_2\text{N}-\text{OH}$	$(\text{HNO}_3)\cdot\text{F}^-$	Commercial standard + IC	30%
Hydroxy methylhydroperoxide	HMHP		$(\text{CH}_4\text{O}_3)\cdot\text{CF}_3\text{O}^-$	Synthesized standard + FTIR	40%
Hydroxyacetone	HAC		$(\text{C}_3\text{H}_6\text{O}_2)\cdot\text{CF}_3\text{O}^-$	Commercial standard + FTIR	40%
Peroxyacetic acid	PAA		$(\text{C}_2\text{H}_4\text{O}_3)\cdot\text{CF}_3\text{O}^-$	Commercial standard + FTIR	40%
C ₄ Hydroxy dicarbonyl	HDC4		$(\text{C}_4\text{H}_6\text{O}_3)\cdot\text{CF}_3\text{O}^-$	Calculated	50%
C ₄ Dihydroxy carbonyl	DHC4		$(\text{C}_4\text{H}_8\text{O}_3)\cdot\text{CF}_3\text{O}^-$	Calculated	50%
Isoprene hydroperoxy-aldehyde	HPALD		$(\text{C}_5\text{H}_8\text{O}_3)\cdot\text{CF}_3\text{O}^-$	Calculated	50%

Isoprene hydroxy-hydroperoxide and isoprene dihydroxy-epoxide	ISOPOOH + IEPOX		$(C_5H_{10}O_3) \cdot CF_3O^-$	Synthesized standards, NMR + gravimetric	40%
Propanone nitrate	PROPNN		$(C_3H_5NO_4) \cdot CF_3O^-$	Separated oxidation mixture + TDLIF	30%
Isoprene hydroxy nitrate	ISOPN		$(C_5H_9NO_4) \cdot CF_3O^-$	Synthesized standard + TDLIF	30%
Methacrolein and Methyl vinyl ketone hydroxy nitrate	MACN/ MVKN		$(C_4H_7NO_5) \cdot CF_3O^-$	Separated oxidation mixture + TDLIF	30%
Isoprene nitroxy hydroperoxide	INP		$(C_5H_9NO_5) \cdot CF_3O^-$	Calculated	50%
Monoterpene nitroxy hydroperoxide	MTNP		$(C_{10}H_{17}NO_5) \cdot CF_3O^-$	Calculated	50%

1

2

1 **Table S2:** Inputs for the revised resistance model used in this work for relevant molecules: H is
 2 the [a] experimental or [b - d] estimated simple Henry's Law coefficient, f_0 is a reactivity factor,
 3 and diffusivity was calculated based on the measured diffusivity of H_2O_2 as defined in the text.

4

Compound	MW (Da)	Diffusivity ($m^2 s^{-1}$)	H ($M atm^{-1}$)	f_0	Calc. V_d ($cm s^{-1}$)	Measured V_d ($cm s^{-1}$)
HCN	27	1.75×10^{-5}	10	[a]	0	0.3 ± 0.1
H_2O_2	34	1.56×10^{-5}	1.1×10^5	[a]	1	5.2 ± 1.1
Formic	46	1.34×10^{-5}	5.6×10^3	[a]	0	1.0 ± 0.4
HNO_3	63	1.15×10^{-5}	3.2×10^5	[a]	1	3.8 ± 1.3
HMHP	64	1.14×10^{-5}	1.3×10^6	[a]	0.1	4.1 ± 1.1
HAC	74	1.06×10^{-5}	2×10^3	[b]	0	1.4 ± 0.5
PAA	76	1.04×10^{-5}	520	[a]	0.1	2.7 ± 0.7
HDC_4	102	9.01×10^{-6}	2×10^3	[b]	0	1.1 ± 0.5
DHC_4	104	8.92×10^{-6}	2×10^3	[b]	0	1.0 ± 0.4
HPALD	116	8.45×10^{-6}	4×10^4	[b]	0	2.4 ± 0.6
ISOPOOH/IEPOX	118	8.37×10^{-6}	7×10^7	[c]	0	2.5 ± 0.6
PROPNN	119	8.34×10^{-6}	1×10^4	[d]	0	1.7 ± 0.6
ISOPN	147	7.50×10^{-6}	5×10^3	[d]	0	1.5 ± 0.6
MACN/ MVKN	149	7.45×10^{-6}	6×10^3	[d]	0	1.5 ± 0.5
INP	163	7.12×10^{-6}	5×10^3	[b]	0	1.3 ± 0.6
MTNP	231	5.98×10^{-6}	1×10^3	[b]	0	0.8 ± 0.4

[a] Mean experimental values from R. Sander (1999), and references therein

[b] Where empirical data are unavailable, similar compounds from R. Sander (1999) were used as proxies (HAC as $C_3H_8O_2$, HDC_4 and DHC_4 as values averaged between butanedione and generic aldehyde, HPALD as a hydroxyaldehyde, INP and MTNP were estimated based on functional groups)

[c] Mean estimates from Marais et al (2013)

[d] Proxy hydroxynitrates from Shepson et al (1996), ISOPN extrapolated to C_5 . See discussion in SI text.

5

1 **Table S3:** Revisions to GEOS-Chem mechanism to reflect kinetic data published after the latest
 2 revision by Mao et al (2013).

Revisions	Reference
Increase ISOPNB +OH rate coefficient by factor of 2.4	Ref. (15)
Decrease MACRN + OH by factor of 11.46	Ref. (41)
Include IEPOX formation and change RO ₂ branching for ISOPNB + OH:	Refs. (15, 42)
<ul style="list-style-type: none"> ISOPNB + OH = 0.88 ISOPNBO₂ + 0.12 IEPOX + 0.12 NO₂ 	
Smaller NOx recycling for ISOPNB RO ₂ radical:	
<ul style="list-style-type: none"> ISOPNBO₂ + NO = 0.249 MVKN + 0.461 MACRN + 0.29 HAC + 0.29 GLYC + 0.71 HCHO + 0.71 HO₂ + 1.29 NO₂ 	Ref. (15)
Decrease rate of ISOPNB + O ₃ to 3 x 10 ⁻¹⁹ cm ³ molec ⁻¹ s ⁻¹	Ref. (15)
Decrease rate of ISOPND + O ₃ rate to 2.8 x 10 ⁻¹⁷ cm ³ molec ⁻¹ s ⁻¹	Ref. (15)
Increase MACRN photolysis rate to 10*J_ONIT1	Ref. (43)

3

1 **Table S4:** Inputs for the base (B) and sensitivity (S) GEOS-Chem simulations, where only the
2 Henry's law factors were adjusted.

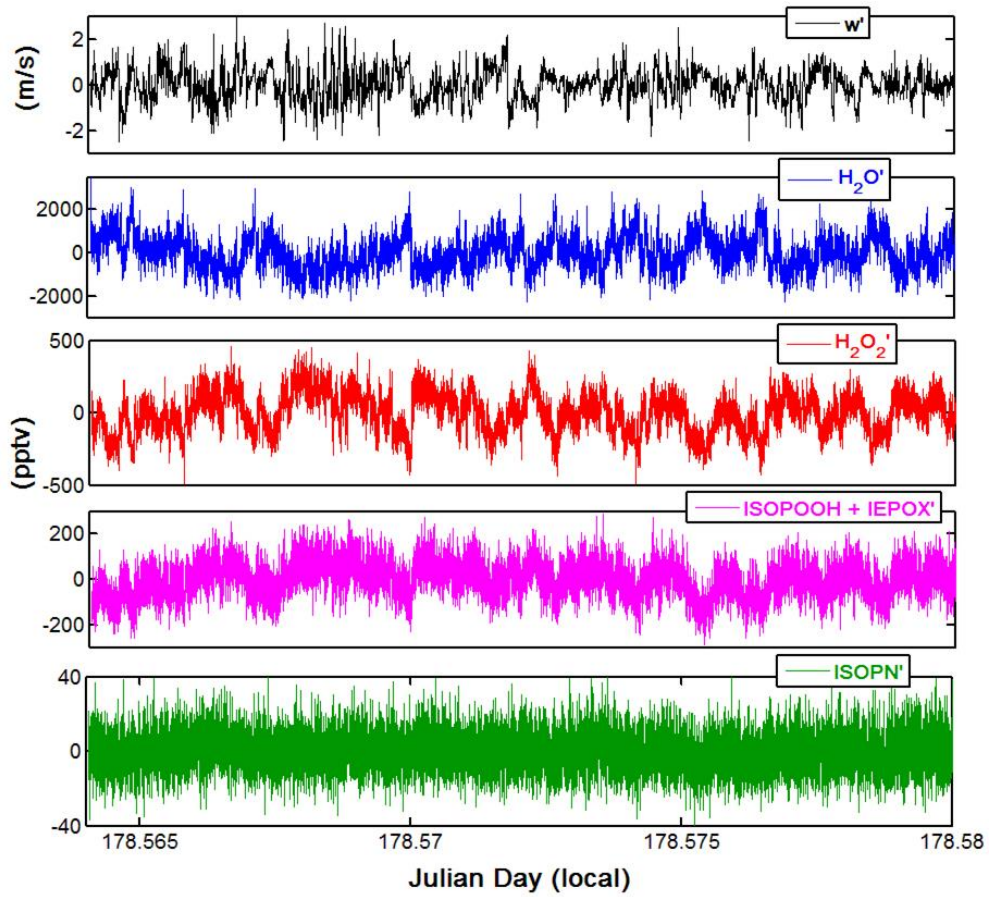
3

Name Index	Henry's Factor (B) (M atm ⁻¹)	Henry's Factor (S) (M atm ⁻¹)	f_0	Molec. Weight (kg mol ⁻¹)
HNO3	1.00E+14	1.00E+14	0	0.063
H2O2	1.00E+05	5.00E+07	1	0.034
ISOPND	1.70E+04	2.00E+06	1	0.147
ISOPNB	1.70E+04	2.00E+06	1	0.147
PROPNN	1.00E+03	5.00E+05	1	0.119
HAC	2.90E+03	1.40E+06	1	0.074
GLYC	4.10E+04	2.00E+07	1	0.06
MACRN	1.70E+04	2.00E+06	1	0.149
MVKN	1.70E+04	2.00E+06	1	0.149
RIP	1.70E+06	1.70E+06	1	0.118
IEPOX	1.30E+08	8.00E+07	1	0.118

4

1

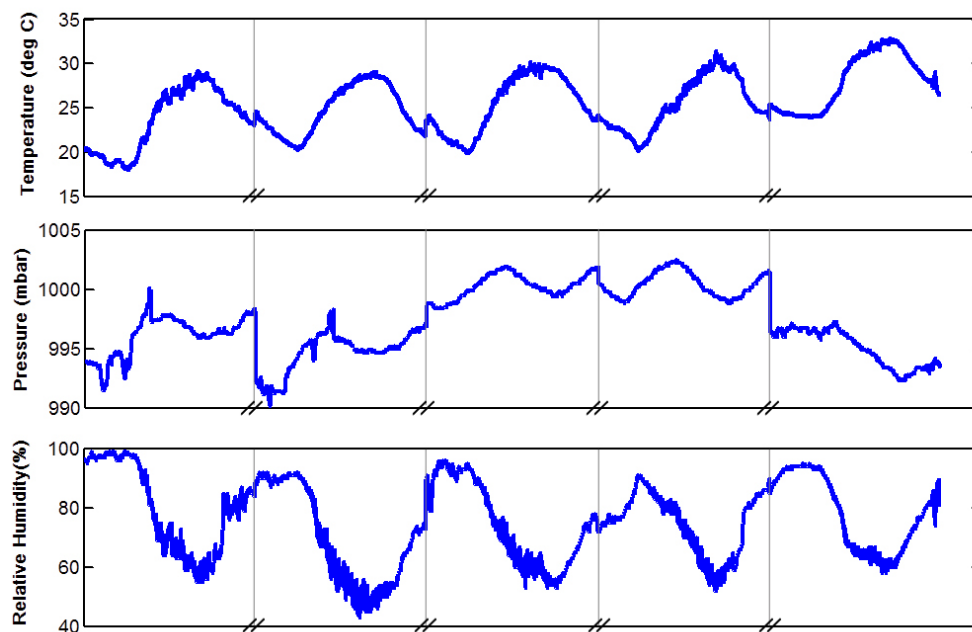
2 **Figures**



3

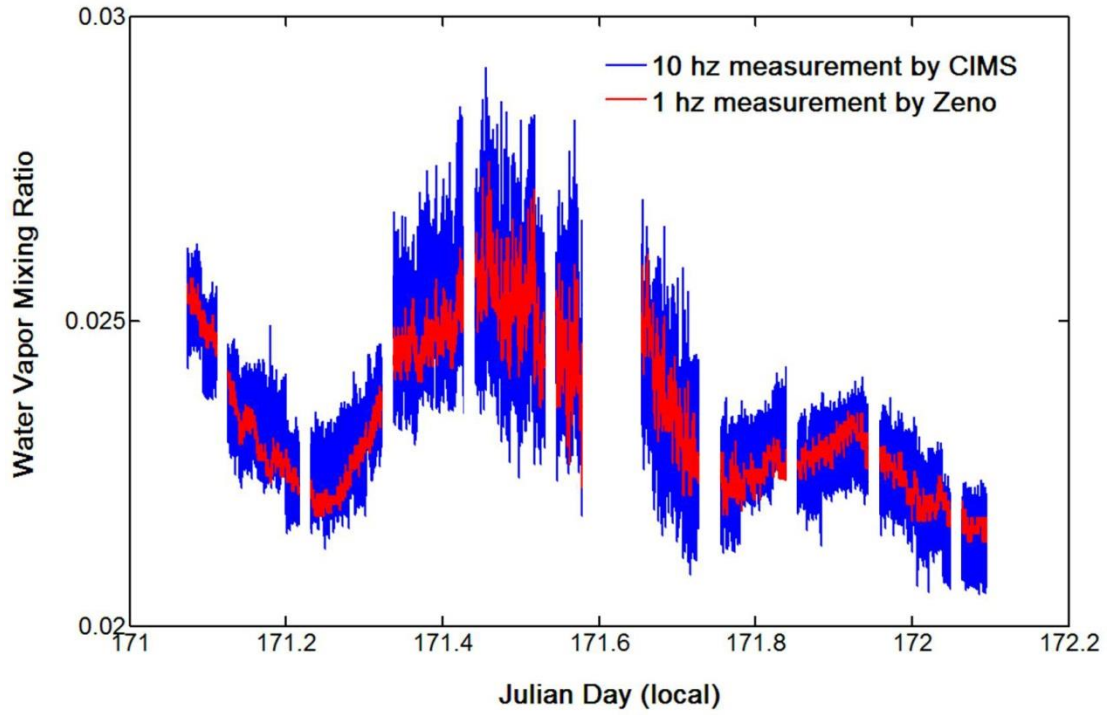
4 **Figure S1:** Prime vectors of vertical wind (w' , black) and CIMS mixing ratios for water vapor
5 (blue), H_2O_2 (red), ISOPHOH + IEPOX (magenta) and ISOPN (green) during a ~ 25 minute
6 segment on June 27.

7



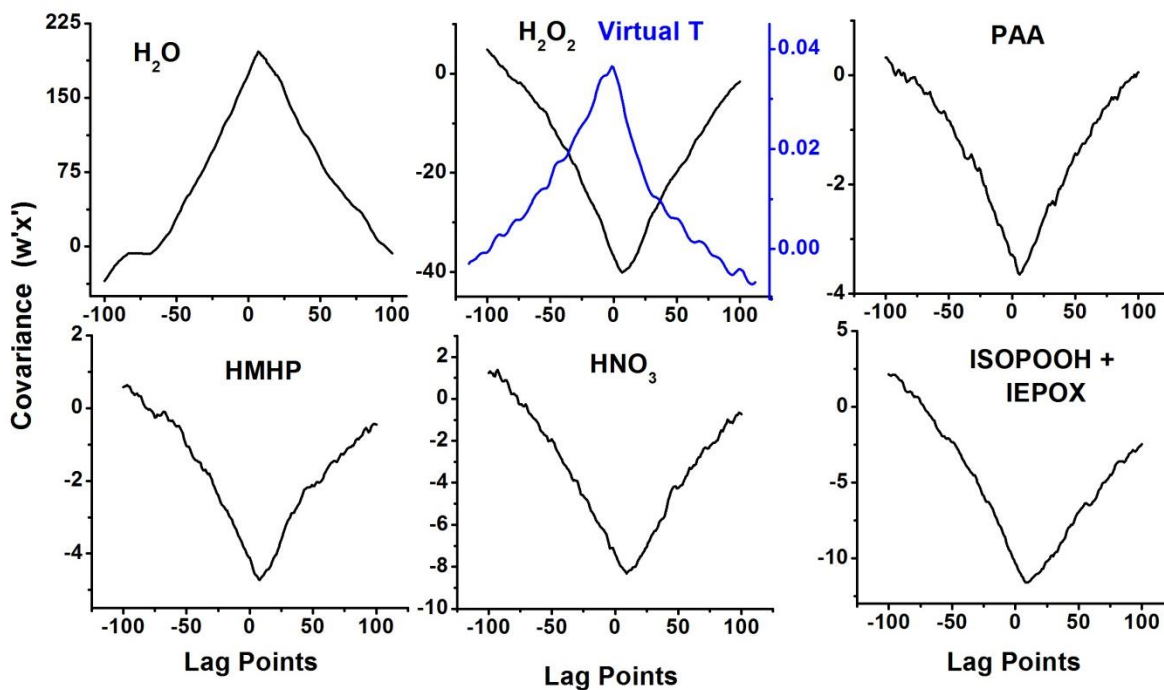
1
2 **Figure S2:** Meteorological parameters on the non-continuous dates included in this study that
3 were used to calculate water vapor fraction for an external calibration of the CIMS water ion
4 measurement.

5
6



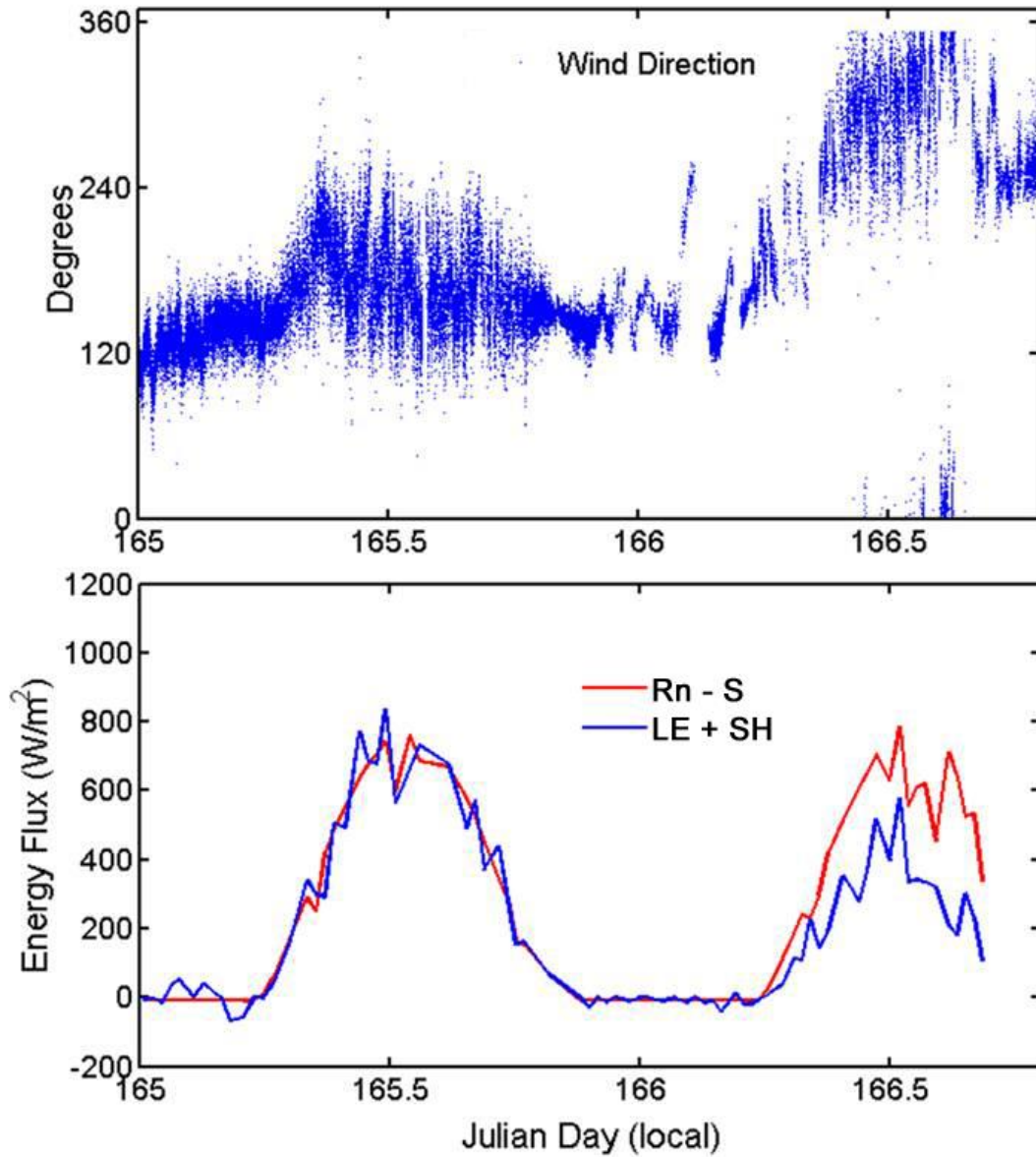
1
2
3
4
5

Figure S3: Water vapor as measured by the CIMS at 10 Hz compared to that measured by the Zeno weather station at 1 Hz.



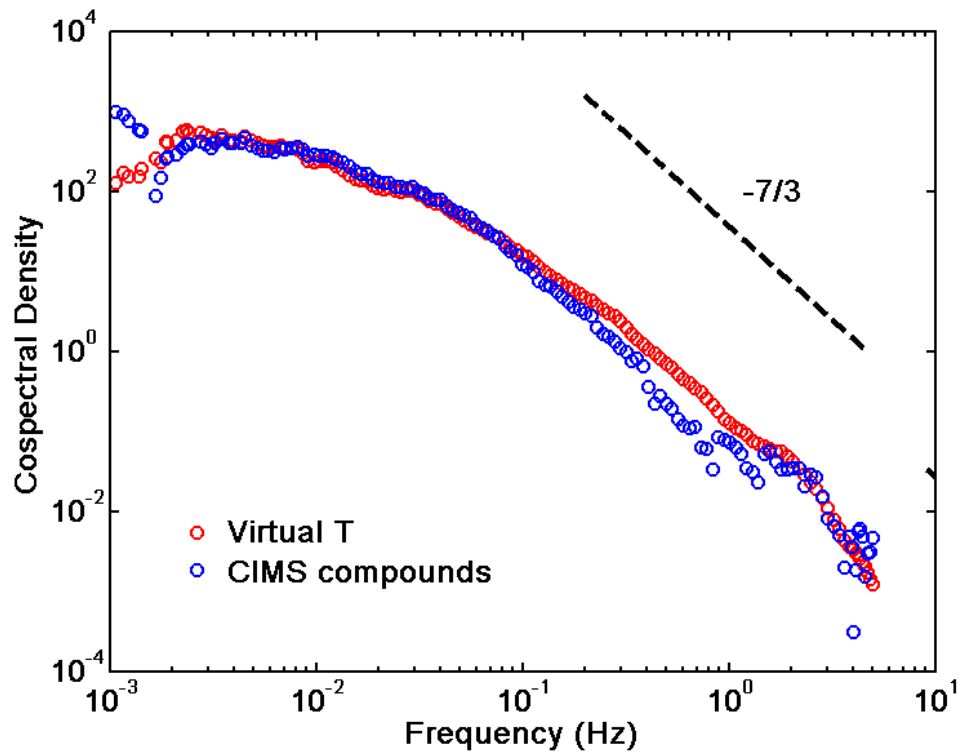
1
2
3
4
5
6
7
8

Figure S4: Representative lag covariance functions of several CIMS compounds and virtual temperature with w , as a function of lag on JD 165, h=14. Units are ppmv m/s for H₂O, °C m/s for T, and pptv m/s otherwise. Extrema locations indicate optimum lag correction times. Each lag point represents ~ 0.1 s. Lag for virtual temperature with respect to w is always zero. Lag for CIMS compounds with respect to w varies from 0.1 – 1.1 s.



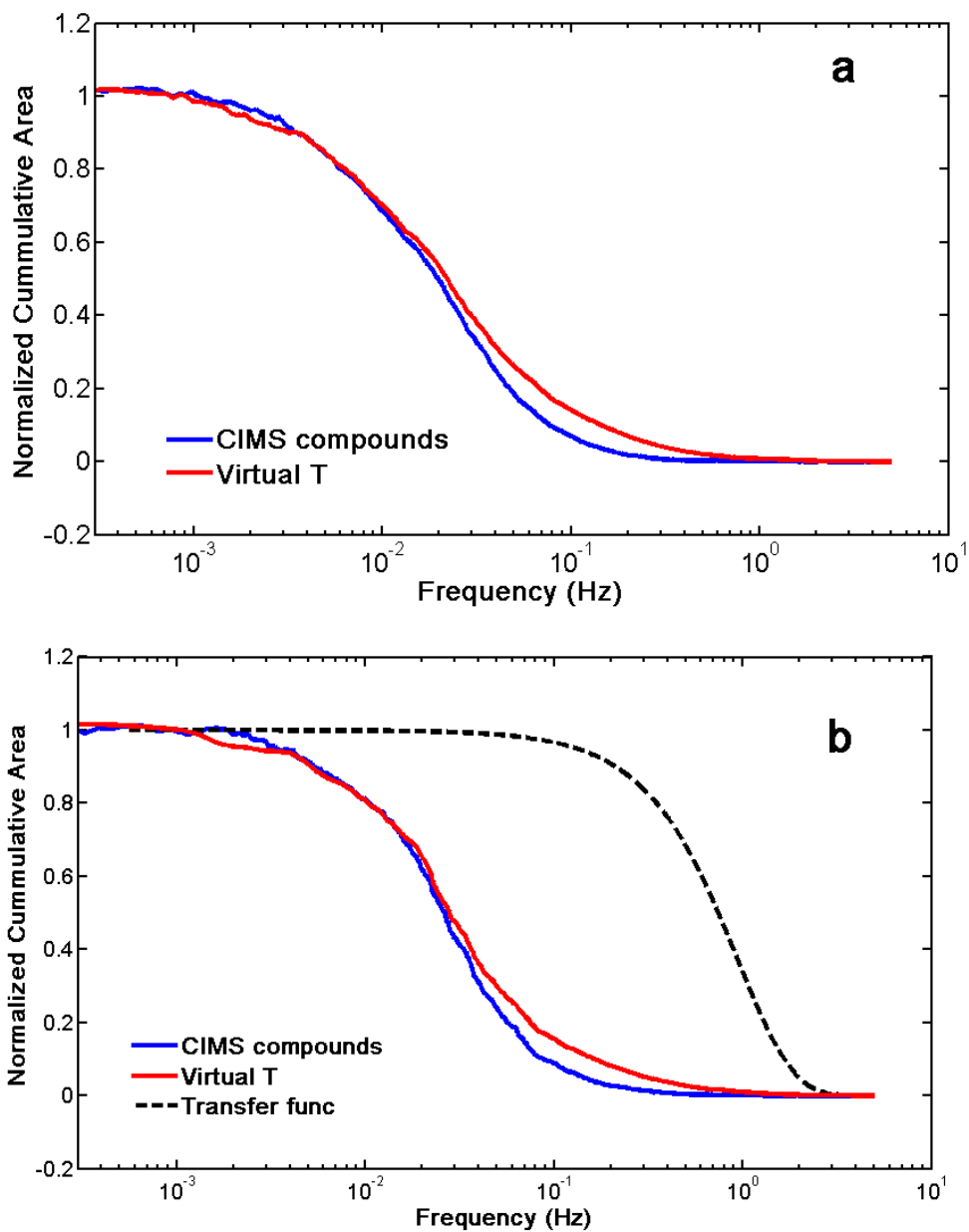
1
 2 **Figure S5:** Energy balance closure for days where wind is northerly (~ 180 degrees) compared
 3 to southerly/southeasterly (320 – 20 degrees).

4
 5



1
 2 **Figure S6:** Representative cospectra for vertical wind (w) with several CIMS compounds and
 3 virtual temperature. Cospectra were calculated for hour 13, binned into 150 frequency bins and
 4 averaged over the all dates included in this study. Dashed black line shows the $f^{-7/3}$ relationship
 5 expected for the inertial subrange ($f > 0.003$ Hz) from surface layer theory.

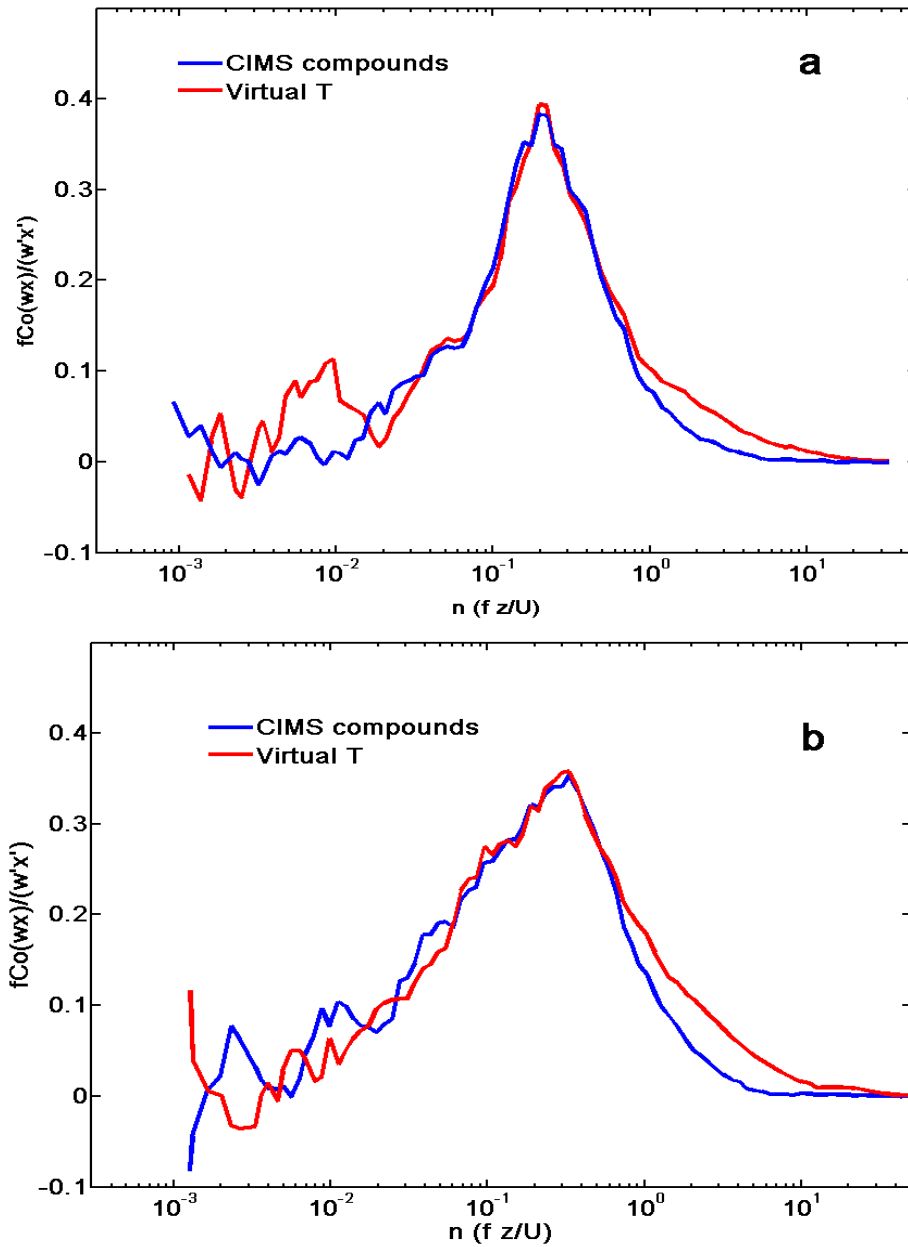
6



1
 2 **Figure S7:** Representative plot of the normalized cumulative sum of unnormalized cospectra
 3 (ogive) for vertical wind (w) with several CIMS compounds and virtual temperature calculated
 4 for (a) hours 9 – 15, averaged over all of the dates included in this study and (b) for JD 165,
 5 superimposed with the normalized transfer function, using mean winds from the day time hours,
 6 calculated for the inlet-sonic separation correction (dashed black line). Ogives were normalized
 7 to their asymptotic value.

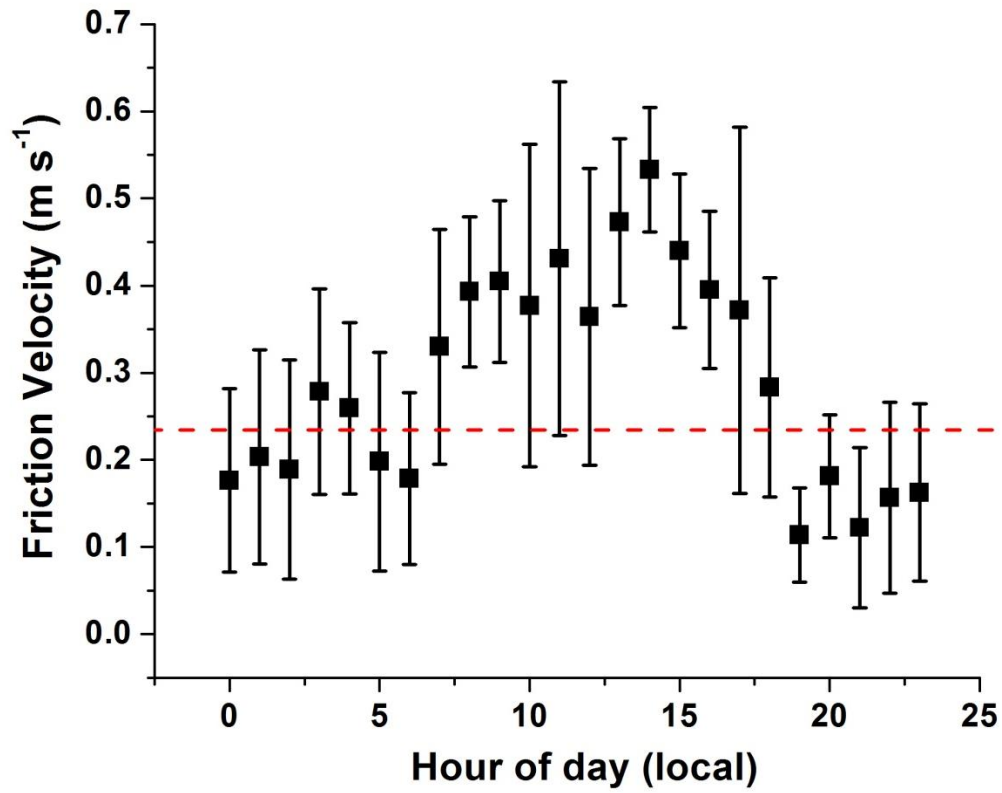
8
 9

1



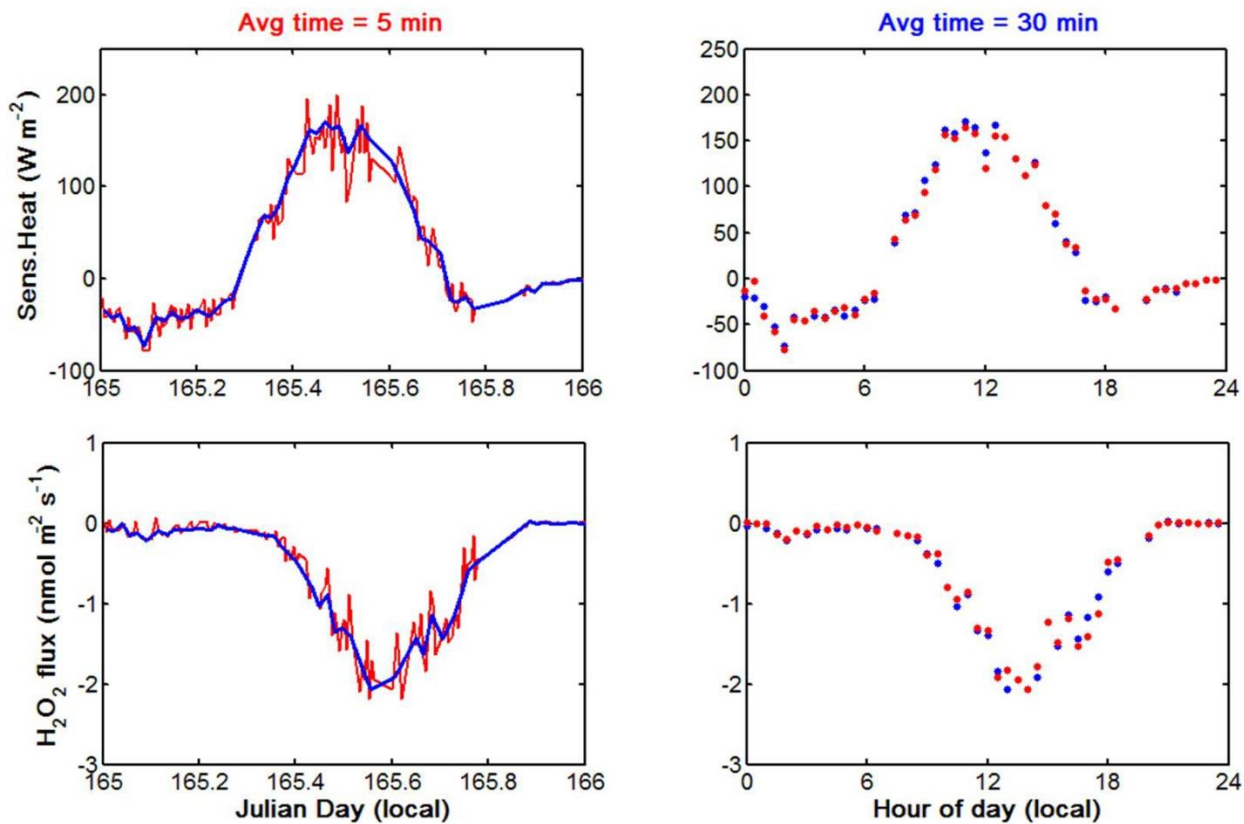
2

3 **Figure S8:** Frequency-weighted covariance-normalized cospectra for vertical wind w with
4 several CIMS compounds and virtual temperature, shown for (a) hours 9 – 15 over the JD 165
5 where $z/U \sim 7$ s and (b) hours 9 – 15 over all flux days where z/U varies.



1

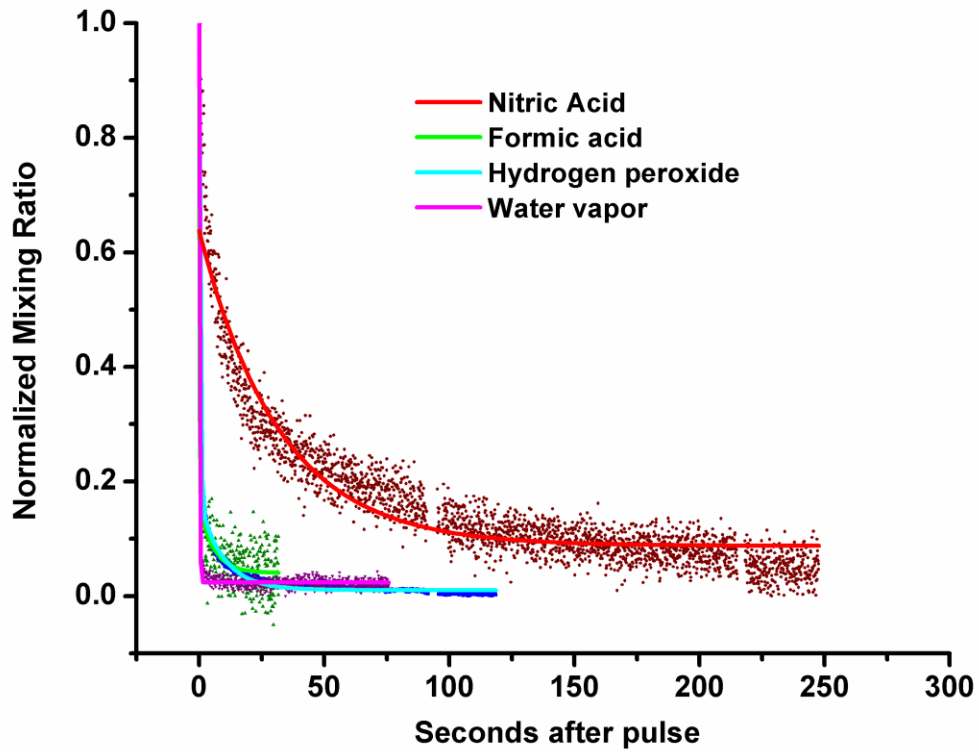
2 **Figure S9:** Friction velocity, as calculated from the momentum flux (see text), averaged over the
 3 dates included in this study. The red line indicates the suggested 0.23 m s^{-1} threshold over which
 4 turbulence can be considered well-developed (44).



1
 2 **Figure S10:** Sensible heat flux and H_2O_2 flux calculated using approximately 30 minute (blue)
 3 and approximately 5 min (red) averaging time intervals. Left panels show raw calculated fluxes
 4 and right panel show calculated fluxes that have been averaged into the same half-hourly bins.

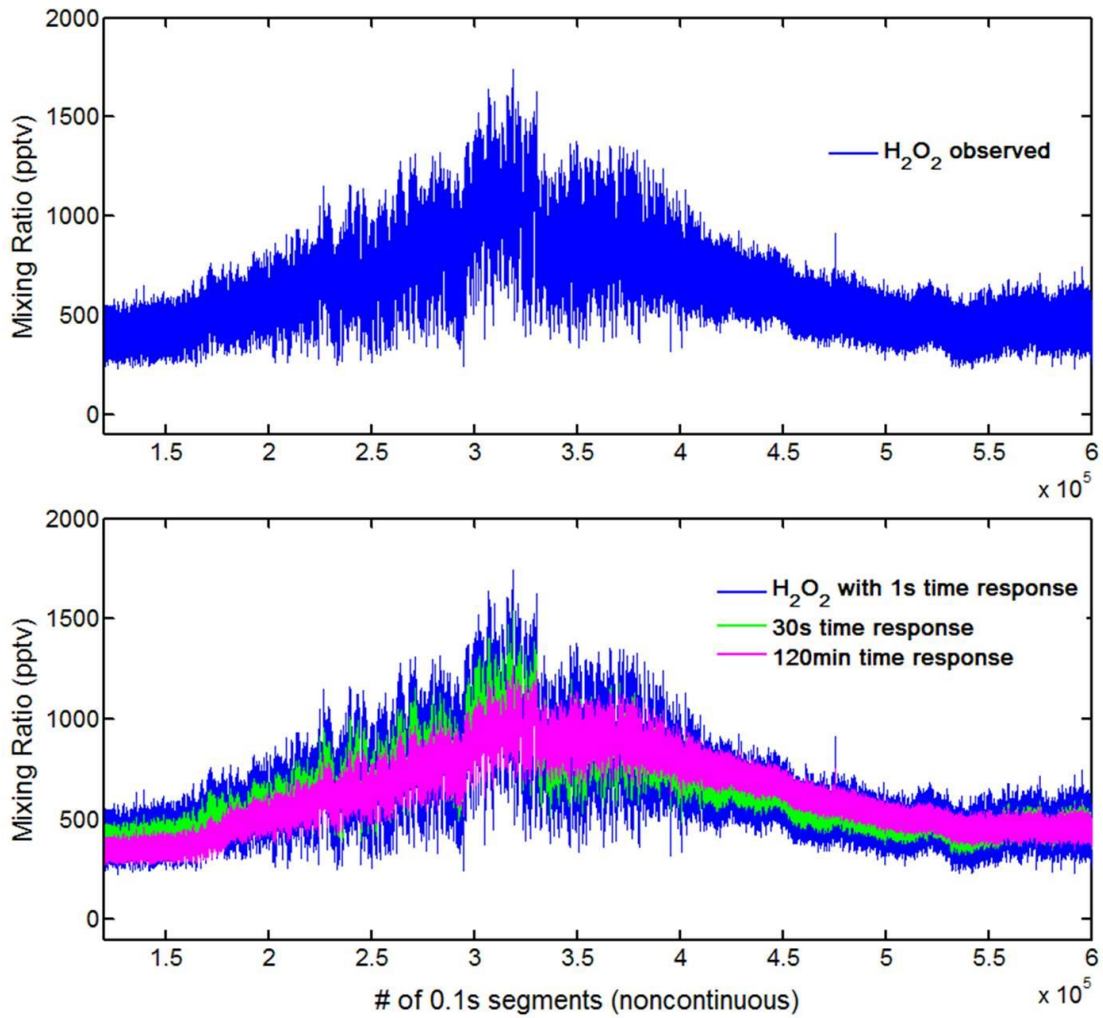
5

1



2

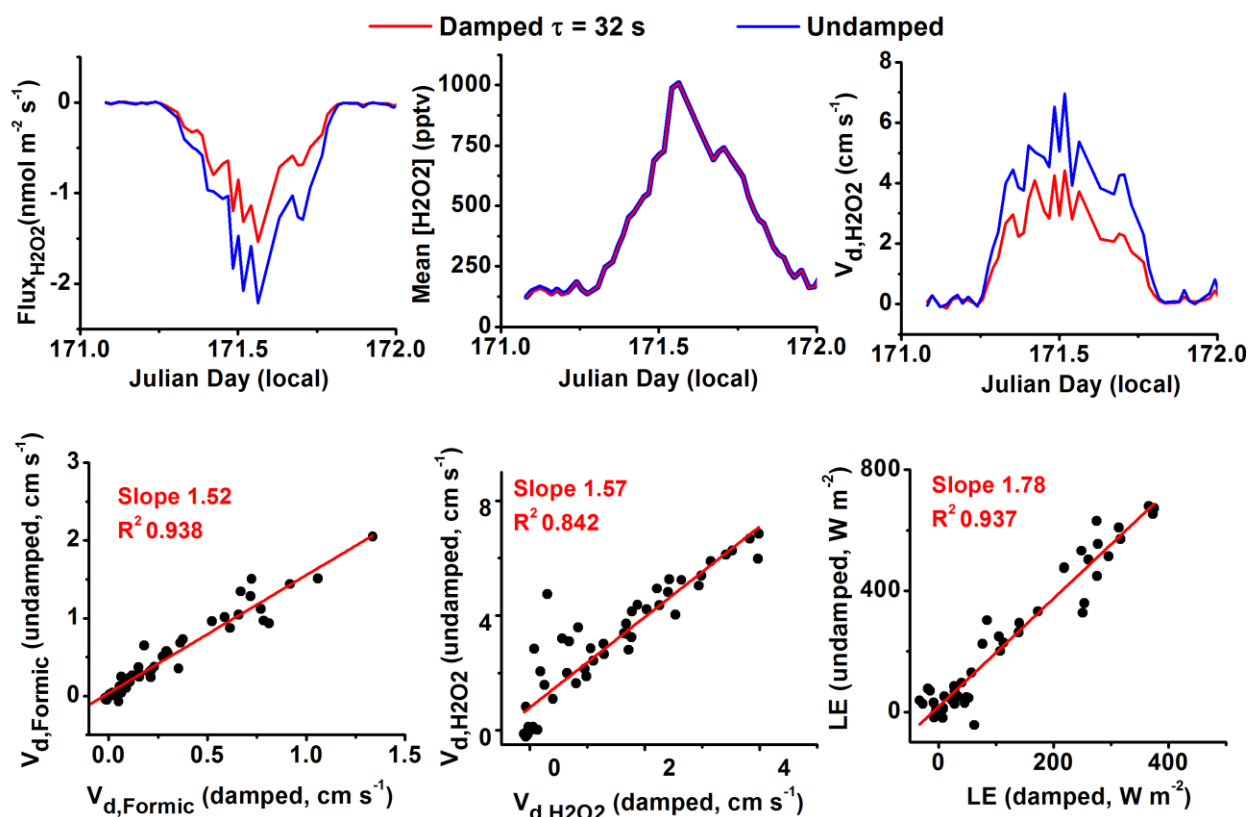
3 **Figure S11:** Decay of CIMS signals from a chemical pulse of individual species, indicating the
4 time response (i.e., “stickiness”) of each species in the CIMS flow region. Time responses were
5 fit with exponential decay functions.



1

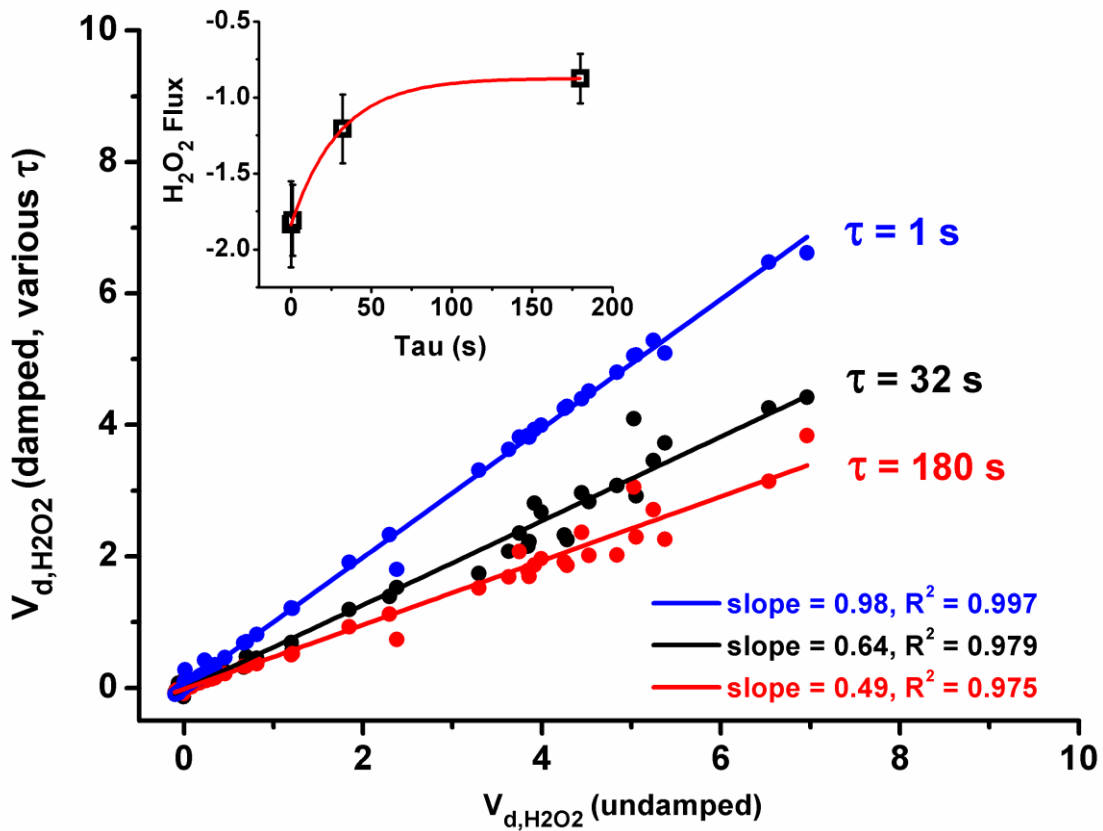
2 **Figure S12:** Top panel: observed H₂O₂ mixing ratio. Bottom panel: H₂O₂ mixing ratio damped
 3 with several time response constants.

4



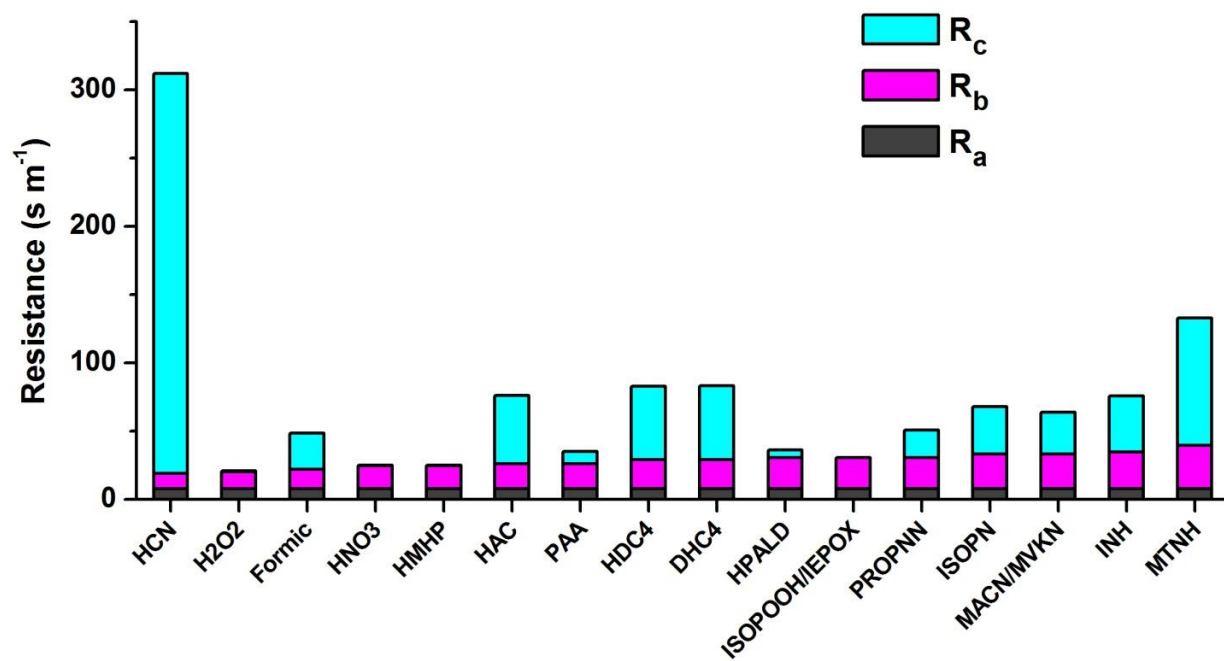
1
 2 **Figure S13:** Top panels (left to right): Hydrogen peroxide flux, mean concentration, and
 3 deposition velocities due to applied inlet dampening with time response factor of 32 seconds
 4 compared to the undamped measurements. Bottom panels (left to right): Comparisons of the
 5 undamped vs. damped values for formic acid V_d , H_2O_2 V_d , and latent heat flux (LE).

6



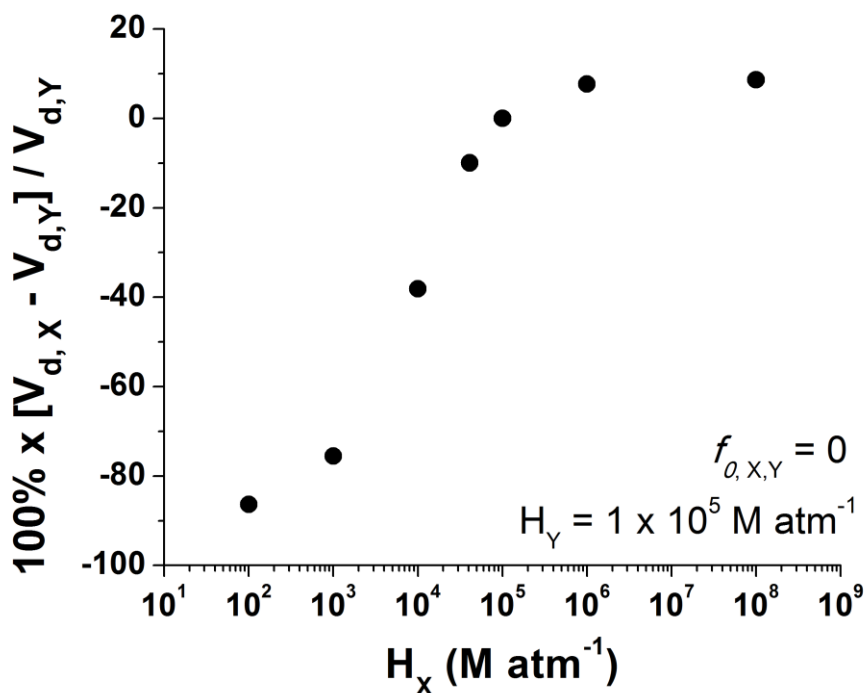
1
 2 **Figure S14:** Representative effect of different time response factors (τ) on the EC fluxes (nmol
 3 $\text{m}^{-2} \text{s}^{-1}$) and V_d (cm s^{-1}) of H_2O_2 . Mean concentrations did not change within a few percent on
 4 this timescale. Insert shows midday flux of H_2O_2 ($h = 12 - 14$) as a function of τ .

5



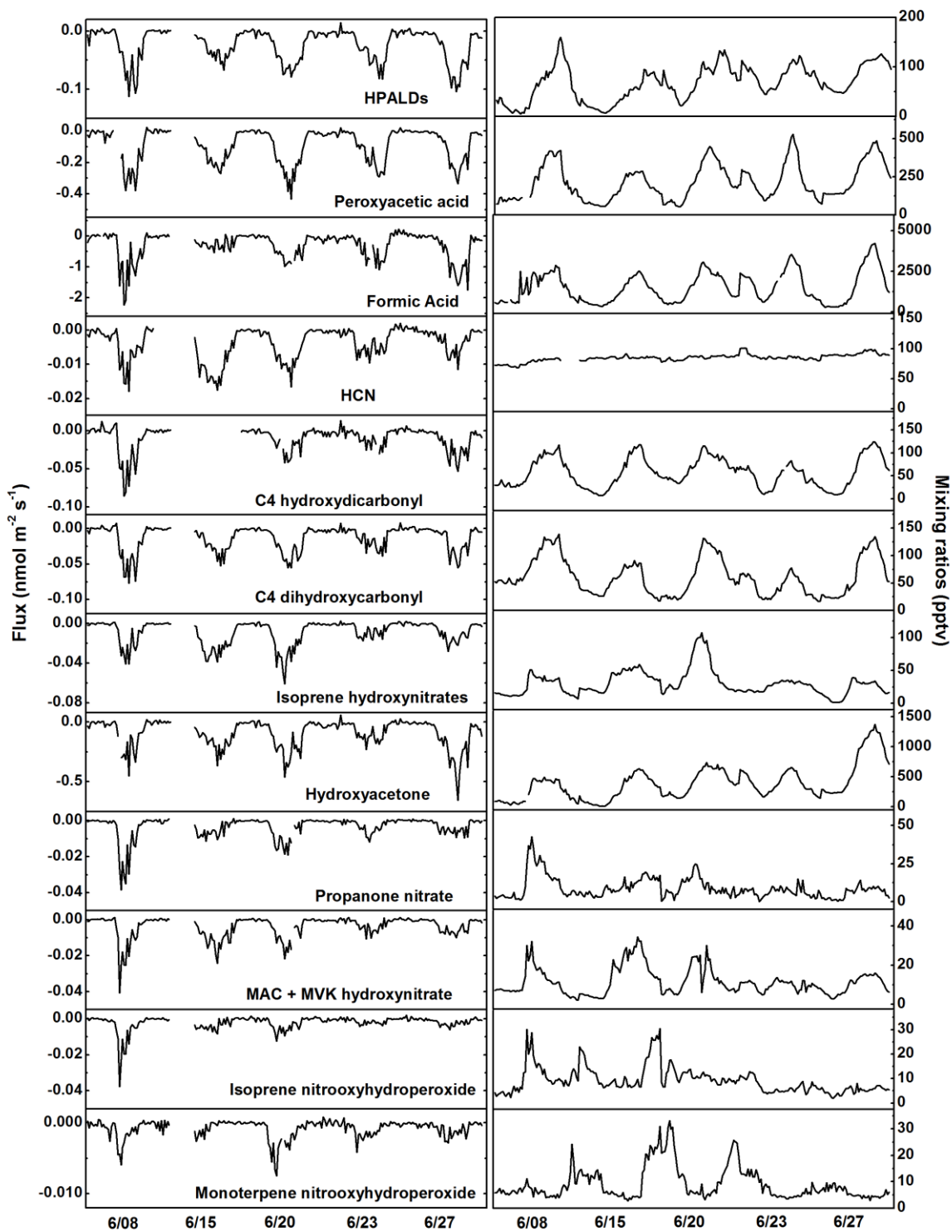
1
 2 **Figure S15:** Modeled resistances using a resistance-in-series scheme (see text) for the chemical
 3 species studied in this work, whose molecular identities are defined in Table S1 and the model
 4 inputs are reported in Table S4.

5

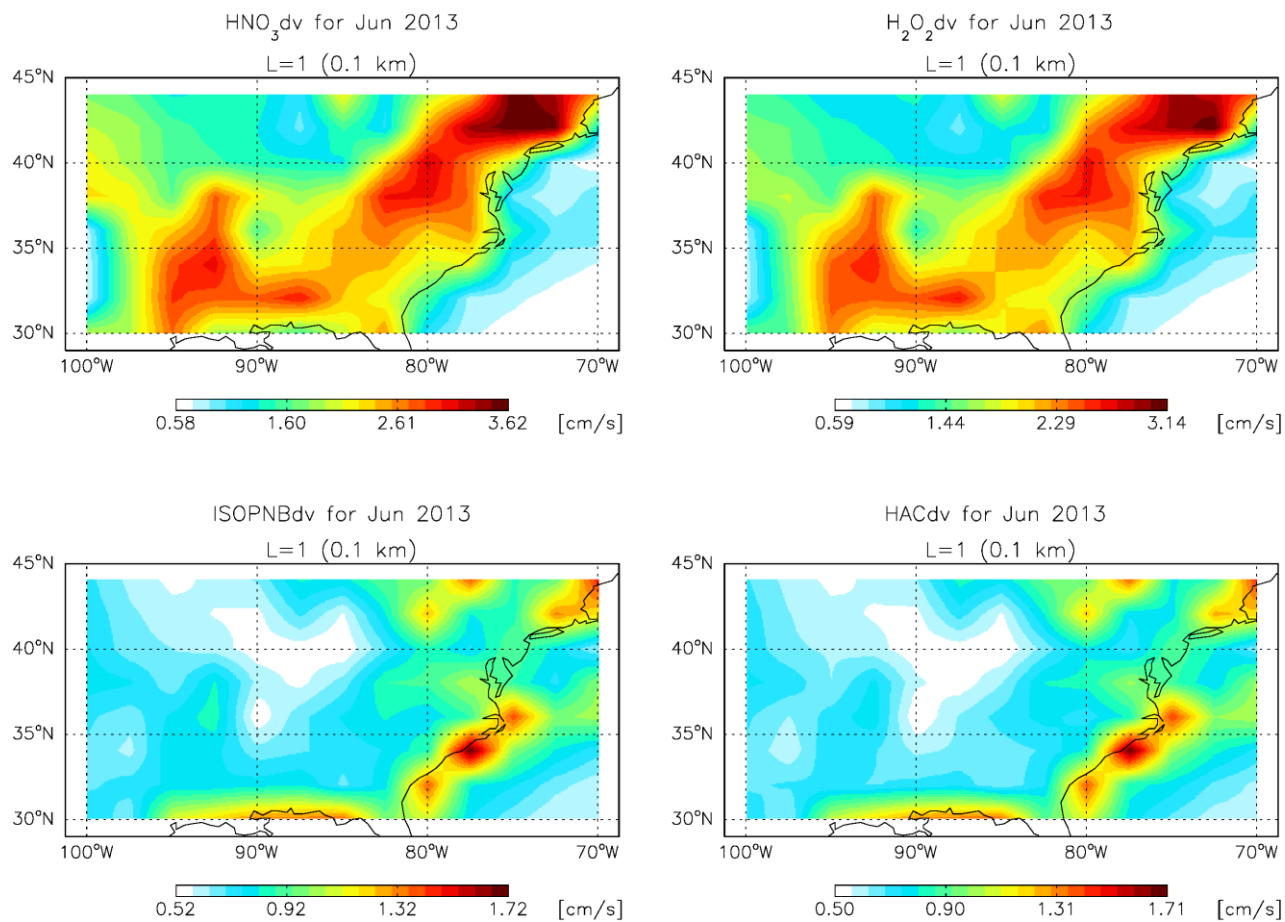


1
 2 **Figure S16:** Sensitivity of the resistance model to uncertainties in Henry's Law coefficient (H)
 3 for a hypothetical compound (Y) with $H = 1 \times 10^5 \text{ M atm}^{-1}$ (water-soluble) and $f_0 = 0$ (non-
 4 reactive). H was varied by several orders of magnitude for another hypothetical compound (X, f_0
 5 = 0), and the percent change in V_d was computed with respect to the reference $V_{d,Y}$.

6



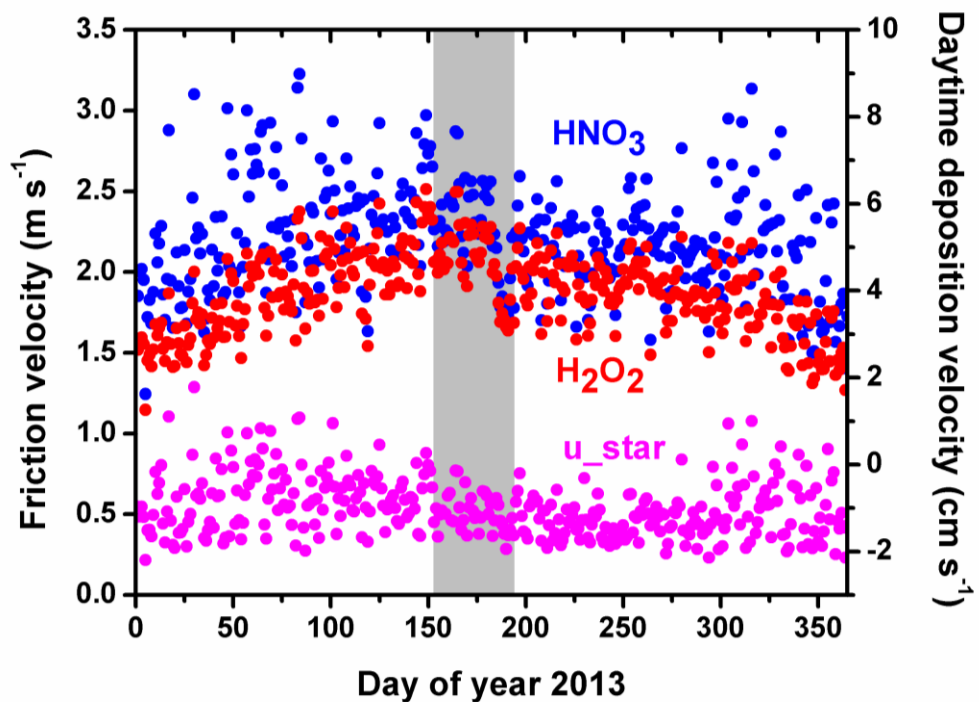
1
 2 **Figure S17:** Fluxes (left panels) and mean mixing ratios (right panels) for the chemical species
 3 for which the data were not shown in the main text. Legends for both panels are shown on the
 4 left.



1
 2 **Figure S18:** Distribution of 24-h average deposition velocities from the sensitivity simulation for
 3 (upper left and clockwise): HNO₃, H₂O₂, ISOPN, and HAC in the Eastern United States grid
 4 boxes. Daytime values are approximately twice the 24-h average.

5

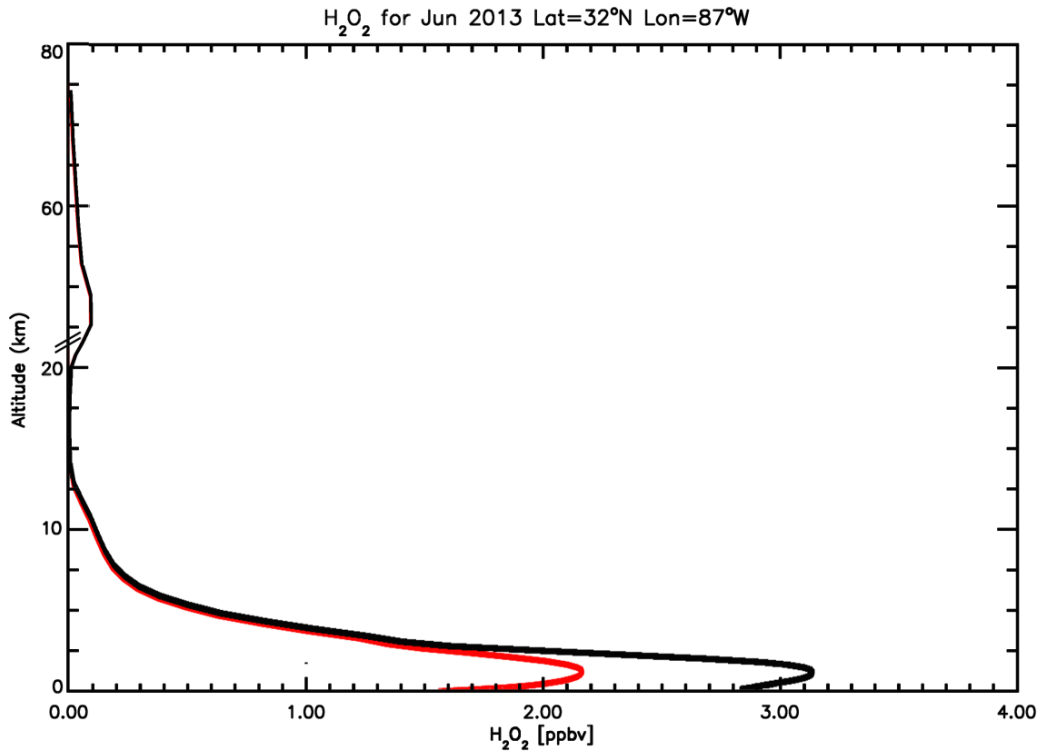
1



2

3 **Figure S19:** Daytime ($h = \text{local noon} \pm 3 \text{ h}$) deposition velocities for HNO_3 and H_2O_2 (right
4 axis) and friction velocity (u_*) from GEOS-FP for every day of the year 2013 at the CTR site.
5 Data were obtained from the year-round sensitivity simulation. The measurement period during
6 SOAS is shown in the gray shaded region.

7



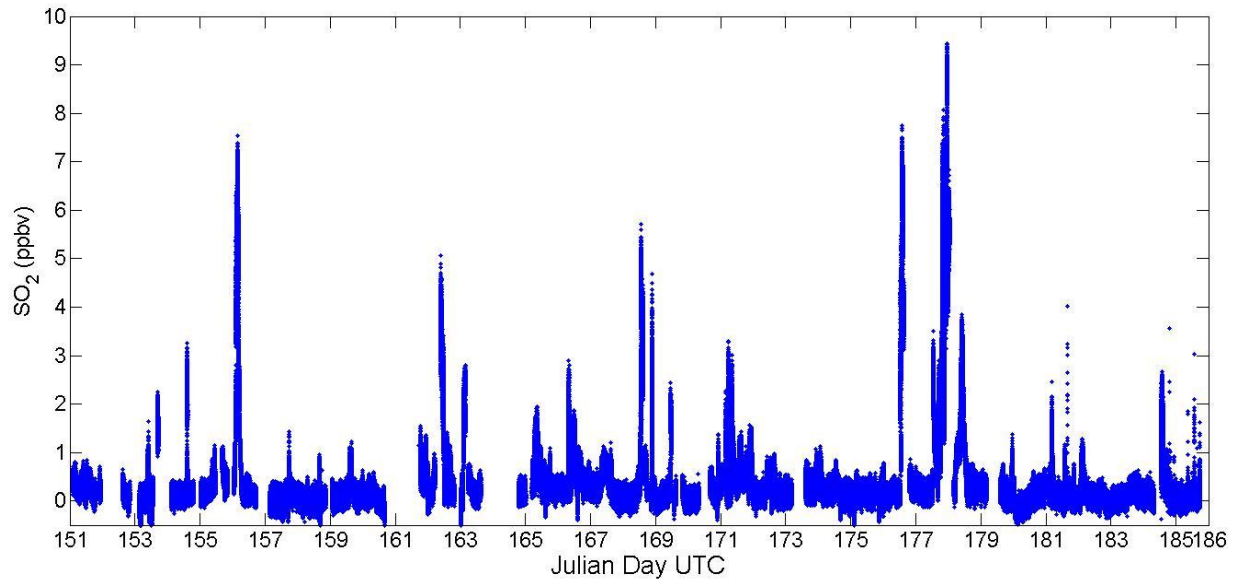
1

2 **Figure S20:** H₂O₂ mixing ratio vertical profile in the base (black) and sensitivity (red) studies for
 3 the CTR site during June 2013. The sensitivity study uses daytime deposition velocities
 4 measured at CTR during SOAS. The surface altitude (shown as “0” in the plot vertical axis)
 5 corresponds to a height of 70 m and values at the measurement height are expected to be 25 –
 6 40% lower than at 70 m. Note the unequal spacing in the vertical axis used to magnify changes
 7 in the boundary layer.

8

9

10



1

2 **Figure S21:** SO₂ mixing ratio observed by TOF-CIMS during the SOAS Campaign.

3

1

2 References:

- 3 1. Crounse JD, McKinney KA, Kwan AJ, & Wennberg PO (2006) Measurement of gas-phase
4 hydroperoxides by chemical ionization mass spectrometry. *Anal. Chem.* 78(19):6726-6732.
- 5 2. Paulot F, *et al.* (2009) Isoprene photooxidation: new insights into the production of acids and
6 organic nitrates. *Atmos. Chem. Phys.* 9(4):1479-1501.
- 7 3. St. Clair JM, McCabe DC, Crounse JD, Steiner U, & Wennberg PO (2010) Chemical ionization
8 tandem mass spectrometer for the in situ measurement of methyl hydrogen peroxide. *Rev. Sci.*
9 *Instrum.* 81(9):094102-094106.
- 10 4. Kaimal JC & Businger JA (1963) A continuous wave sonic anemometer-thermometer. *J. Appl.*
11 *Meteorol.* 2(1):156-164.
- 12 5. Su T & Chesnavich WJ (1982) Parametrization of the ion-polar molecule collision rate constant
13 by trajectory calculations. *J. Chem. Phys.* 76(10):5183-5185.
- 14 6. Garden AL, *et al.* (2009) Calculation of conformationally weighted dipole moments useful in
15 ion-molecule collision rate estimates. *Chem. Phys. Lett.* 474(1):45-50.
- 16 7. Rothman LS, *et al.* (2009) The HITRAN 2008 molecular spectroscopic database. *J. Quant.*
17 *Spectrosc. Ra.* 110(9):533-572.
- 18 8. Griffith DWT (1996) Synthetic calibration and quantitative analysis of gas-phase FT-IR spectra.
19 *Appl. Spectrosc.* 50(1):59-70.
- 20 9. Orlando JJ, Tyndall GS, Vereecken L, & Peeters J (2000) The atmospheric chemistry of the
21 acetonoxo radical. *J. Phys. Chem. A* 104(49):11578-11588.
- 22 10. Fry JL, *et al.* (2006) OH-Stretch vibrational spectroscopy of hydroxymethyl hydroperoxide. *J.*
23 *Phys. Chem. A* 110(22):7072-7079.
- 24 11. Sharpe SW, Sams RL, & Johnson TJ (2002) The PNNL quantitative IR database for infrared
25 remote sensing and hyperspectral imaging. *Applied Imagery Pattern Recognition Workshop,*
26 *2002. Proceedings. 31st*, pp 45-48.
- 27 12. Bates KH, *et al.* (2014) Gas phase production and loss of isoprene epoxydiols. *J. Phys. Chem. A*
28 118(7):1237-1246.
- 29 13. Nguyen TB, *et al.* (2014) Organic aerosol formation from the reactive uptake of isoprene
30 epoxydiols (IEPOX) onto non-acidified inorganic seeds. *Atmos. Chem. Phys.* 14(7):3497-3510.
- 31 14. Paulot F, *et al.* (2009) Unexpected epoxide formation in the gas-phase photooxidation of
32 isoprene. *Science* 325(5941):730-733.
- 33 15. Lee L, Teng AP, Wennberg PO, Crounse JD, & Cohen RC (2014) On rates and mechanisms of
34 OH and O₃ Reactions with isoprene-derived hydroxy nitrates. *J. Phys. Chem. A* 118:1622-1637.
- 35 16. Foken T & Wichura B (1996) Tools for quality assessment of surface-based flux measurements.
36 *Agr. Forest Meteorol.* 78(1-2):83-105.
- 37 17. Mahrt L (1998) Nocturnal boundary-layer regimes. *Bound.-Lay. Meteorol.* 88(2):255-278.
- 38 18. Ollinger SV, *et al.* (2008) Canopy nitrogen, carbon assimilation, and albedo in temperate and
39 boreal forests: Functional relations and potential climate feedbacks. *Proc. Nat. Acad. Sci.*
40 105(49):19336-19341.
- 41 19. Kaminsky KZ & Dubayah R (1997) Estimation of surface net radiation in the boreal forest and
42 northern prairie from shortwave flux measurements. *J. Geophys. Res.* 102(D24):29707-29716.
- 43 20. Kaimal JC & Finnigan JJ (1994) *Atmospheric boundary layer flows: their structure and*
44 *measurement* (Oxford University Press).
- 45 21. Wolfe GM, *et al.* (2009) Eddy covariance fluxes of acyl peroxy nitrates (PAN, PPN and MPAN)
46 above a Ponderosa pine forest. *Atmos. Chem. Phys.* 9(2):615-634.
- 47 22. Papale D (2006) Towards a standardized processing of Net Ecosystem Exchange measured with
48 eddy covariance technique: algorithms and uncertainty estimation. *Biogeoscience* 3:571 - 583.

- 1 23. Foken T, Leuning R, Oncley SR, Mauder M, & Aubinet M (2012) Corrections and data quality
2 control. *Eddy Covariance*, (Springer), pp 85-131.
- 3 24. Webb EK, Pearman GI, & Leuning R (1980) Correction of flux measurements for density effects
4 due to heat and water vapour transfer. *Q. J. Roy. Meteor. Soc.* 106(447):85-100.
- 5 25. Moore C (1986) Frequency response corrections for eddy correlation systems. *Bound.-Lay.*
6 *Meteorol.* 37(1-2):17-35.
- 7 26. Bey I, *et al.* (2001) Global modeling of tropospheric chemistry with assimilated meteorology:
8 Model description and evaluation. *J. Geophys. Res.* 106(D19):23073-23095.
- 9 27. Wesely ML (1989) Parameterization of surface resistances to gaseous dry deposition in regional-
10 scale numerical models. *Atmos. Environ.* 23(6):1293-1304.
- 11 28. Karl T, *et al.* (2010) Efficient atmospheric cleansing of oxidized organic trace gases by
12 vegetation. *Science* 330(6005):816-819.
- 13 29. Wesely M & Hicks B (2000) A review of the current status of knowledge on dry deposition.
14 *Atmos. Environ.* 34(12):2261-2282.
- 15 30. Dyer A (1974) A review of flux-profile relationships. *Bound.-Lay. Meteorol.* 7(3):363-372.
- 16 31. Jensen NO & Hummelshøj P (1995) Derivation of canopy resistance for water vapour fluxes over
17 a spruce forest, using a new technique for the viscous sublayer resistance. *Agr. Forest Meteorol.*
18 73(3-4):339-352.
- 19 32. Jensen NO & Hummelshøj P (1997) Erratum to Derivation of canopy resistance for water vapour
20 fluxes over a spruce forest, using a new technique for the viscous sublayer resistance. *Agr. Forest*
21 *Meteorol.* 85(3):289.
- 22 33. McMurtrie R & Keyes F (1948) A measurement of the diffusion coefficient of hydrogen peroxide
23 vapor into air. *J. Amer. Chem. Soc.* 70(11):3755-3758.
- 24 34. Hall B, Claiborn C, & Baldocchi D (1999) Measurement and modeling of the dry deposition of
25 peroxides. *Atmos. Environ.* 33(4):577-589.
- 26 35. Valverde-Canossa J, *et al.* (2006) First measurements of H₂O₂ and organic peroxides surface
27 fluxes by the relaxed eddy-accumulation technique. *Atmos. Environ.* 40:55-67.
- 28 36. Ganzeveld L, Valverde-Canossa J, Moortgat GK, & Steinbrecher R (2006) Evaluation of
29 peroxide exchanges over a coniferous forest in a single-column chemistry-climate model. *Atmos.*
30 *Environ.* 40(0):68-80.
- 31 37. Shepson PB, Mackay E, & Muthuramu K (1996) Henry's Law constants and removal processes
32 for several atmospheric β -hydroxy alkyl nitrates. *Environ. Sci. Technol.* 30(12):3618-3623.
- 33 38. Treves K, Shragina L, & Rudich Y (2000) Henry's Law constants of some beta-, gamma-, and
34 delta-hydroxy alkyl nitrates of atmospheric interest. *Environ. Sci. Technol.* 34(7):1197-1203.
- 35 39. Sander R (1999) Compilation of Henry's Law constants for inorganic and organic species of
36 potential importance in environmental chemistry. (Max-Planck Institute of Chemistry, Air
37 Chemistry Dept, Mainz, Germany).
- 38 40. Meyers T, Huebert B, & Hicks B (1989) HNO₃ deposition to a deciduous forest. *Bound.-Lay.*
39 *Meteorol.* 49(4):395-410.
- 40 41. Jenkin M, *et al.* (2012) Development and chamber evaluation of the MCM v3. 2 degradation
41 scheme for β -caryophyllene. *Atmos. Chem. Phys.* 12(11):5275-5308.
- 42 42. Jacobs MI, Burke WJ, & Elrod MJ (2014) Kinetics of the reactions of isoprene-derived
43 hydroxynitrates: gas phase epoxide formation and solution phase hydrolysis. *Atmos. Chem. Phys.*
44 *Discuss.* 14(8):12121-12165.
- 45 43. Müller J-F, Peeters J, & Stavrakou T (2014) Fast photolysis of carbonyl nitrates from isoprene.
46 *Atmos. Chem. Phys.* 14(5):2497-2508.
- 47 44. Reichstein M, *et al.* (2005) On the separation of net ecosystem exchange into assimilation and
48 ecosystem respiration: review and improved algorithm. *Global Change Biol.* 11(9):1424-1439.

49